

# PlanetProfile: Self-consistent interior structure modeling for terrestrial bodies in Python

Marshall J Styczinski<sup>1</sup>, Steven D Vance<sup>1</sup>, and Mohit Melwani Daswani<sup>2</sup>

<sup>1</sup>Jet Propulsion Laboratory

<sup>2</sup>Jet Propulsion Laboratory, California Institute of Technology

December 7, 2022

## Abstract

The open-source PlanetProfile framework was developed to investigate the interior structure of icy moons based on self-consistency and comparative planetology. The software, originally written in Matlab, relates observed and measured properties, assumptions such as the type of materials present, and laboratory equation-of-state data through geophysical and thermodynamic models to evaluate radial profiles of mechanical, thermodynamic, and electrical properties, as self-consistently as possible. We have created a Python version of PlanetProfile. In the process, we have made optimization improvements and added parallelization and parameter-space search features to utilize fast operation for investigating unresolved questions in planetary geophysics, in which many model inputs are poorly constrained. The Python version links to other scientific software packages, including for evaluating equation-of-state data, magnetic induction calculations, and seismic calculations. Physical models in PlanetProfile have been reconfigured to improve self-consistency and generate the most realistic relationships between properties. Here, we describe the software design and algorithms in detail, summarize models for major moons across the outer solar system, and discuss new inferences about the interior structure of several bodies. The high values and narrow uncertainty ranges reported for the axial moments of inertia for Callisto, Titan, and Io are difficult to reconcile with self-consistent models, requiring highly porous rock layers equivalent to incomplete differentiation for Callisto and Titan, and a high rock melt fraction for Io. This effect is even more pronounced with the more realistic models in the Python version. Radial profiles for each model and comparison to prior work are provided as Zenodo archives.

# ***PlanetProfile*: Self-consistent interior structure modeling for terrestrial bodies in Python**

**M. J. Styczinski<sup>1,2</sup>, S. D. Vance<sup>2</sup>, and M. Melwani Daswani<sup>2</sup>**

<sup>1</sup>NASA Postdoctoral Program Fellow, Jet Propulsion Laboratory, California Institute of Technology,  
Pasadena, California, USA

<sup>2</sup>Jet Propulsion Laboratory, California Institute of Technology, Pasadena, California, USA

## **Key Points:**

- Radial models of planetary interiors are generated from bulk properties based on geophysical models, lab data, and minimal assumptions
- Bodies with a high moment of inertia such as Callisto require low-density rocks, which we model with a high effective porosity
- Cross-comparison of magnetic induction and gravity analysis demonstrates a narrowed parameter space for the properties of Europa's ocean

## Abstract

The open-source *PlanetProfile* framework was developed to investigate the interior structure of icy moons based on self-consistency and comparative planetology. The software, originally written in Matlab, relates observed and measured properties, assumptions such as the type of materials present, and laboratory equation-of-state data through geophysical and thermodynamic models to evaluate radial profiles of mechanical, thermodynamic, and electrical properties, as self-consistently as possible. We have created a Python version of *PlanetProfile*. In the process, we have made optimization improvements and added parallelization and parameter-space search features to utilize fast operation for investigating unresolved questions in planetary geophysics, in which many model inputs are poorly constrained. The Python version links to other scientific software packages, including for evaluating equation-of-state data, magnetic induction calculations, and seismic calculations. Physical models in *PlanetProfile* have been reconfigured to improve self-consistency and generate the most realistic relationships between properties. Here, we describe the software design and algorithms in detail, summarize models for major moons across the outer solar system, and discuss new inferences about the interior structure of several bodies. The high values and narrow uncertainty ranges reported for the axial moments of inertia for Callisto, Titan, and Io are difficult to reconcile with self-consistent models, requiring highly porous rock layers equivalent to incomplete differentiation for Callisto and Titan, and a high rock melt fraction for Io. This effect is even more pronounced with the more realistic models in the Python version. Radial profiles for each model and comparison to prior work are provided as Zenodo archives.

## Plain Language Summary

The software package *PlanetProfile* was developed in order to connect measurable properties of planetary bodies to each other and determine how planetary interiors might be structured. We adapted the existing Matlab version of *PlanetProfile* to Python and improved it in many ways in the process, to better investigate scientific questions. Python is more widely available, and *PlanetProfile* now connects better to other scientific software packages capable of relating measurements and observations to the interior structure of planetary bodies such as large moons. *PlanetProfile* is now more adaptable for new scientific investigations and for adding features, includes more realistic relationships between pressures, temperatures, and physical properties of materials, and is optimized

for studies that require a wide variety of models to be run. These improvements make *PlanetProfile* a powerful tool that will become more useful as new features are added. We summarize our models for the major large moons in the outer solar system and provide output files detailing each model. In creating these models, we found that bulk properties for Io, Callisto, and Titan are difficult to include self-consistently, which suggests that the reported values may contain errors.

## 1 Introduction

Liquid water oceans are common among the large moons of the outer planets (Nimmo & Pappalardo, 2016). Evidence supporting present-day subsurface oceans comes from a wide variety of sources, including measurements of magnetic fields (Kivelson et al., 2000), gravity fields (Nimmo et al., 2016), geodesy (Beuthe et al., 2016), libration (Thomas et al., 2016), and more. Water is a requirement for all known life on Earth (Cockell et al., 2016; Westall & Brack, 2018), so finding it in great abundance is an exciting development in the search for life elsewhere. Understanding the physical and chemical conditions present in these oceans is therefore critical to understanding whether they may be habitable (Vance et al., 2018) and what types of organisms may be found there (Rothschild & Mancinelli, 2001).

The long tradition of geophysical investigation of Earth has demonstrated the importance of synthesizing information from a variety of observational and theoretical methods for understanding the properties of material layers at inaccessible depths (*e.g.*, Dziewonski & Anderson, 1981). Constraining the conditions of interior layers of icy moons requires a similar synthesis. Compared to studies at Earth, measurements from the outer solar system will always be sparse, thus forcing a greater emphasis on global-scale modeling efforts.

There are myriad ways to combine the available information into models of layered interior structure. Although planetary bodies are always inherently 3D in their structure, it is instructive to approximate the bodies as spherically symmetric, as this will generally be true to first order for most physical properties. Lateral variations can then be added as perturbations to the symmetric, radial model. The open-source software framework *PlanetProfile* has emerged from such efforts to model the interior structure of icy

---

Available on GitHub at <https://github.com/NASA-Planetary-Science/PlanetProfile>.

moons (Vance et al., 2014, 2016). The guiding principle upon which *PlanetProfile* is built is self-consistency: a harmonious relationship between all model inputs, assumptions, and outputs, such that there is no internal inconsistency. Many physical properties of planetary bodies, especially in the outer solar system, are unknown and must be assumed. However, among the properties that are measured or rigorously inferred, self-consistent modeling provides a crucial link needed to derive bounding constraints that satisfy known conditions and span the breadth of reasonable assumptions. Self-consistent models thus represent a robust method for combining measurements from multiple investigations into coherent first-order constraints on interior structure.

*PlanetProfile* was originally written in Matlab and focused on Europa, Ganymede, Callisto, Enceladus, and Titan (Vance et al., 2018). The software combines bulk properties such as mass, axial moment of inertia, and surface radius, along with surface properties such as mean temperature and pressure, with several assumed properties to calculate depth profiles of geophysically important quantities, such as temperature, pressure, density, seismic wave velocities, electrical conductivity using geophysical models, thermodynamic models, and laboratory equation-of-state (EOS) measurements. We have converted the entirety of the software to Python, with the intent to improve accessibility and organization of the framework. The Supplemental Information includes a comparison of Python *PlanetProfile* outputs for the models analogous to those studied by Vance et al. (2018). These comparison models are also provided as a Zenodo archive: <https://doi.org/10.5281/zenodo.7318029>.

We have generalized the approach of *PlanetProfile* to be applicable to waterless bodies (*e.g.*, Io) and constructed models for major moons spanning the outer solar system and Pluto based on constraints available in the literature. In the process of converting the software to Python, we have made many improvements to the self-consistent modeling approach, optimization of the computational architecture, and integration with related software packages available in Python. The primary purpose of this work is to describe the improved self-consistent modeling approach and the features we have implemented to enable applicability to many solar system bodies (Section 2). We also present model results for bodies across the outer solar system (Section 3: Figures 5–9 and Tables 5–9) and discuss new insights obtained using the updated solution method in Section 4. In particular, Io, Callisto, and Titan are challenging to model self-consistently, owing to likely solid-state mantle convection and/or incomplete differentiation. High rock

porosities are required in these models to match spacecraft observations of their bulk properties and gravity field, simulating a lack of differentiation or partial melt (see Section 4).

### 1.1 Note About Matching and Uncertainty of the Axial Moment of Inertia

Degree-2 coefficients in the gravitational potential of a body (*e.g.*,  $J_2$  and  $C_{22}$ ) relate to the configuration of mass within the body, and therefore can be used to probe the interior structure. These coefficients can be measured via the Doppler shift in radio signals exchanged with spacecraft during flybys of the body (Anderson et al., 1998). It is typical to then assume that the body is in hydrostatic equilibrium—*i.e.*, the layers do not support stresses capable of maintaining a shape departing from the lowest-gravitational-energy configuration, as in a fluid with no rigidity. In the hydrostatic case, the Radau–Darwin approximation (Rambaux & Castillo-Rogez, 2013) can be applied to determine the axial moment of inertia  $C$ , often reported in dimensionless units as  $C/MR^2$  (and simply called the moment of inertia, MoI). This quantity is useful as a metric to constrain the interior structure of planetary bodies, as it can be calculated from depth profiles of mass density and compared to the measured value. For a spherical body of uniform mass density,  $C/MR^2 = 2/5$ . The lower the measured value of  $C/MR^2$ , the more concentrated is the mass inside the body. In this way, measurements of the gravitational field of numerous moons (*e.g.*, Anderson, Jacobson, Lau, et al., 2001; Anderson et al., 1998, 1996; Anderson, Jacobson, McElrath, et al., 2001) have been used to infer the MoI for these bodies. However, departure from hydrostatic conditions is likely (*e.g.*, McKinnon, 2006; Gao & Stevenson, 2013). Applying the Radau–Darwin approximation in these cases will result in a true MoI less than the reported value by as much as a few percent (Gao & Stevenson, 2013). Gao and Stevenson (2013) consider a 3% variation as within the uncertainty in gravitational coefficients of Callisto and other moons, though they also note that the hydrostatic assumption can result in MoI values as much as 10% away from the true value. To account for such variation, in *PlanetProfile* the upper and lower bounds for MoI matching can be independently set to a wider range than the tight  $1\sigma$  uncertainties quoted in the literature.

**Table 1.** Data sources for equation-of-state (EOS) measurements and the range over which the measurements can be interpolated in pressure  $P$ , temperature  $T$ , and salinity  $w$ . Units for salinity are in g solute per kg total solution. The spline fits used to interpolate tabular data can be used to extrapolate to a greater range of  $P$ ,  $T$ , and  $w$  conditions in most cases. No spline fit is used for Seawater EOS data; Seawater ocean models are therefore limited to bodies the size of Europa (radius 1560 km) and smaller.

Material	EOS evaluation	$P$ valid (MPa)	$T$ valid (K)	$w$ valid (g kg <sup>-1</sup> )
Ice (Ih, II, III, V, VI)	<i>SeaFreeze</i> <sup>abc</sup>	0 – 2300	73 – 500	-
CH <sub>4</sub> clathrate (phase stability)	Fit to data from literature <sup>d</sup>	0.1 – 20	200 – 290	-
CH <sub>4</sub> clathrate (density and seismic)	Parameterization from literature <sup>e</sup>	30 – 98	253 – 288	-
CH <sub>4</sub> clathrate (thermodynamic)	Parameterization from literature <sup>f</sup>	0.1 – 100	5 – 292	-
Liquid water (pure)	<i>SeaFreeze</i> <sup>g</sup>	0.1 – 2300	240 – 500	-
MgSO <sub>4</sub> (aq)	Parameterization and data from literature <sup>hij</sup>	0.1 – 800	253 – 373	0 – 231
Seawater	<i>Gibbs Seawater (TEOS-10)</i> <sup>k</sup>	0.1 – 100	250 – 373	0 – 50
Rocky layers (“silicates”)	<i>Perple_X</i> <sup>l</sup>	0.1 – 14000	273 – 2000	-
Iron + sulfur (metallic) core	<i>Perple_X</i> <sup>l</sup>	0.1 – 14000	273 – 2000	-

<sup>a</sup> Available on GitHub (and PyPI): <https://github.com/Bjournaux/SeaFreeze>

<sup>b</sup> Feistel and Wagner (2006) (Ih)

<sup>c</sup> Journaux et al. (2020) (II, III, V, VI)

<sup>d</sup> Choukroun et al. (2010)

<sup>e</sup> Helgerud et al. (2009)

<sup>f</sup> Ning et al. (2015)

<sup>g</sup> Bollengier et al. (2019)

<sup>h</sup> Vance et al. (2014) (phase transitions)

<sup>i</sup> Vance and Brown (2013) (physical properties)

<sup>j</sup> Vance et al. (2018) (electrical properties)

<sup>k</sup> McDougall and Barker (2011), <https://www.teos-10.org/software.htm>

<sup>l</sup> Connolly (2009), <https://www.perplex.ethz.ch/>. *Perple\_X* uses mineral data from multiple sources—see Table 2.

**Table 2.** Sources of EOS data from the literature used for minerals implemented by *Perple\_X*.

Model name	Mineral type	Data source
Atg(PN)	Antigorite	Padrón-Navarta et al. (2013)
Bi(HGP)	Biotite	(Holland et al., 2018)
Chl(HP)	Chlorite	(Holland et al., 1998)
COH-Fluid	CO <sub>2</sub> –CH <sub>4</sub> –H <sub>2</sub> –CO–H <sub>2</sub> O– H <sub>2</sub> S–SO <sub>2</sub> –N <sub>2</sub> –NH <sub>3</sub> fluid with linear subdivisions	(Connolly & Galvez, 2018)
Cpx(HGP)	Clinopyroxene	(Holland et al., 2018)
Do(HP)	Dolomite-ankerite	(Holland & Powell, 1998)
Gt(HGP)	Garnet	(Holland et al., 2018)
M(HP)	Magnesite-siderite-rhodochrosite	(Holland & Powell, 1998)
melt(HGP)	Generic silicate melt	(Holland et al., 2018)
Mica(CF)	Fe–Mg–K–Na mica	(Chatterjee & Froese, 1975; Holland & Powell, 1998)
O(HGP)	Olivine	(Holland et al., 2018)
Omph(GHP)	Omphacite	(Green et al., 2007)
Opx(HGP)	Orthopyroxene	(Holland et al., 2018)
Pl(JH)	Plagioclase	(Jennings et al., 2016)
Pu	Pumpellyite	(Holland & Powell, 2011) <sup>a</sup>
Sp(HGP)	Spinel	(Holland et al., 2018)
Stlp	Stilpnomelane	(Holland & Powell, 2011) <sup>a</sup>
T	Talc	(Holland & Powell, 2011) <sup>a</sup>

<sup>a</sup> Implemented with the DEW17HP622ver\_elements *Perple\_X* data file—see  
[https://www.perplex.ethz.ch/perplex\\_thermodynamic\\_data\\_file.html](https://www.perplex.ethz.ch/perplex_thermodynamic_data_file.html).



## 2 Self-Consistent Model Design

*PlanetProfile* is designed around self-consistency. This principle is achieved and maintained by making as few assumptions as possible while still enabling a determination of the physical properties as a function of depth that result from measured and assumed inputs. Physical properties are determined for each material from interpolation of laboratory measurements of these properties over many different temperatures and pressures, known as equation-of-state (EOS) measurements. Table 1 lists the software sources of EOS evaluation available in *PlanetProfile* for each currently supported material type. The material type within each major layer (rocks, core, *etc.*) is assumed to be uniform, except in cases where porosity is modeled (Section 2.4). In *PlanetProfile*, “silicates” is used as a shorthand to refer to any rocky material, and includes a variety of minerals. The minerals modeled in *PlanetProfile* using *Perple\_X* are listed along with the data sources in Table 2.

Table 3 lists the measured inputs required by *PlanetProfile*, along with values used for selected moons in this work. Measured inputs are used to match the bulk physical characteristics of the modeled body. Table 4 lists the assumed inputs required by *PlanetProfile* along with the range or set of values we have modeled. The assumed inputs are required in order to have enough information to solve for the unknown properties. Certain critical assumptions—namely the ocean solute composition, salinity, and melting temperature (if an ocean is present)—must be supposed from inferences based on laboratory measurements (*e.g.*, Zolotov & Kargel, 2009), surface reflectance spectra (*e.g.*, Trumbo et al., 2019), indirect sampling (*e.g.*, Glein & Waite, 2020), plausible building block composition (*e.g.*, Melwani Daswani et al., 2021), *etc.* Methane clathrate hydrate (sI) is optionally modeled as a conductive lid, an ice shell underplate, or throughout the ice shell, with stability determined from a parameterization to data from Choukroun et al. (2010).

To make the problem tractable, each material layer (ice, rock, *etc.*) is divided into a number of discrete layers. The number of layers sets the resolution of the output model and controls the total run time, typically 0.5–10 s. The primary output from *PlanetProfile* is an ASCII text file containing columns describing physical properties of each discrete layer as a function of depth (and radius). This output is referred to as a profile.

**Table 3.** Measured bulk properties required as inputs by *PlanetProfile*, along with values used in default models for varied example bodies. Several properties, such as surface radius, temperature, and pressure, are used directly as calculation starting points. Other properties, such as mass and axial moment of inertia (MoI), are used to determine profile validity and select a matching, self-consistent profile. A full list of the bulk properties for default models included in *PlanetProfile* is detailed in Tables 10–13.

Property	Io	Ganymede	Enceladus
Radius $R$ (km) <sup>a</sup>	1821.49	2631.2	252.1
Total mass $M$ (kg)	$8.932 \times 10^{22}$ <sup>b</sup>	$1.4819 \times 10^{23}$ <sup>b</sup>	$1.08022 \times 10^{20}$ <sup>c</sup>
Axial MoI $C/MR^2$ <sup>d</sup>	$0.37685^{+0.00035}_{-0.01166}$ <sup>e</sup>	$0.3115^{+0.0028}_{-0.0121}$ <sup>f</sup>	$0.335^{+0.001}_{-0.011}$ <sup>g</sup>
Surface pressure $P_{\text{surf}}$ (MPa)	0	0	0
Surface temperature $T_{\text{surf}}$ (K)	110	110	75

<sup>a</sup> Mean radii from Archinal et al. (2018)

<sup>b</sup> Hussmann et al. (2006)

<sup>c</sup> Jacobson et al. (2006)

<sup>d</sup> Lower values increased by 3% of mean value per Gao and Stevenson (2013)

<sup>e</sup> Anderson, Jacobson, Lau, et al. (2001)

<sup>f</sup> Schubert et al. (2004)

<sup>g</sup> Iess et al. (2014)

**Table 4.** Assumed properties required as inputs by *PlanetProfile* for calculation of self-consistent depth profiles. Default inputs are listed for the same example bodies as in Table 3. Ice bottom temperatures are each selected to be consistent with the range of ice shell thickness supported by published studies. Surface heat flux is calculated for icy bodies from the thermal conductivity of the ice shell conductive lid; this quantity is an input for waterless bodies. Rock compositions are consistent with a differentiated body, such that the total elemental inventory of rock + core matches the modeled chondritic material, assuming all free fluids (volatiles) are lost to the hydrosphere or escape from the body. A full list of bulk properties for the default models included in *PlanetProfile* are detailed in Tables 10–13.

Property	Io	Ganymede	Enceladus
Ocean composition and salinity $w$	N/A	Pure H <sub>2</sub> O	10 g kg <sup>-1</sup> Seawater
Ice bottom temperature $T_b$	N/A	258.86 K	272.4578 K
Surface heat flux $q_{\text{surf}}$	0.14 W m <sup>-2</sup>	N/A	N/A
Rock composition	CV chondrite	CM chondrite	Comet 67P/C–G
Core FeS/(Fe+FeS) ratio $x_{\text{FeS}}$	12.5 wt% FeS	20 wt% FeS	not modeled
Ice porosity in vacuum $\phi_{\text{ice}}$	N/A	not modeled	not modeled
Ice pore closure pressure $P_{c,\text{ice}}$	-	-	-
Rock porosity in vacuum $\phi_{\text{rock}}$	70 vol%	not modeled	32 vol%
Rock pore closure pressure $P_{c,\text{rock}}$	750 MPa	-	350 MPa

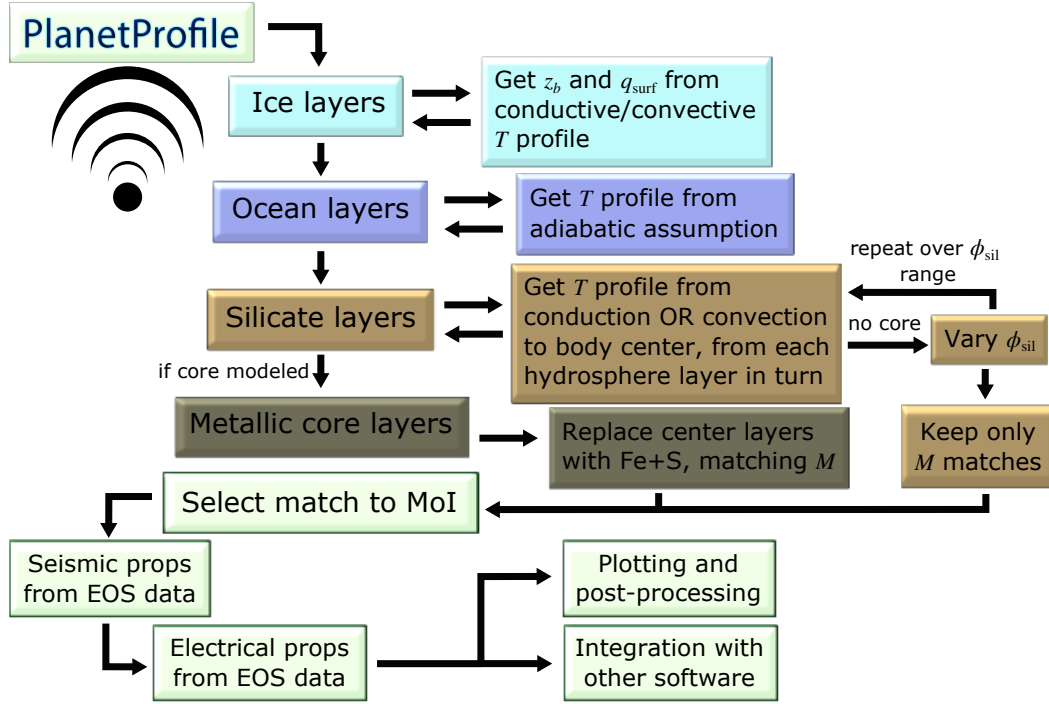


**Figure 1.** Overall design of *PlanetProfile* self-consistent models of interior structure. For waterless bodies, ice/ocean layers are skipped and  $q_{\text{surf}}$  is an input.  $z_b$ : ice shell thickness;  $q_{\text{surf}}$ : surface heat flux;  $T$ : layer temperature;  $\phi_{\text{rock}}$ : rock porosity at 0 pressure;  $M$ : total body mass.

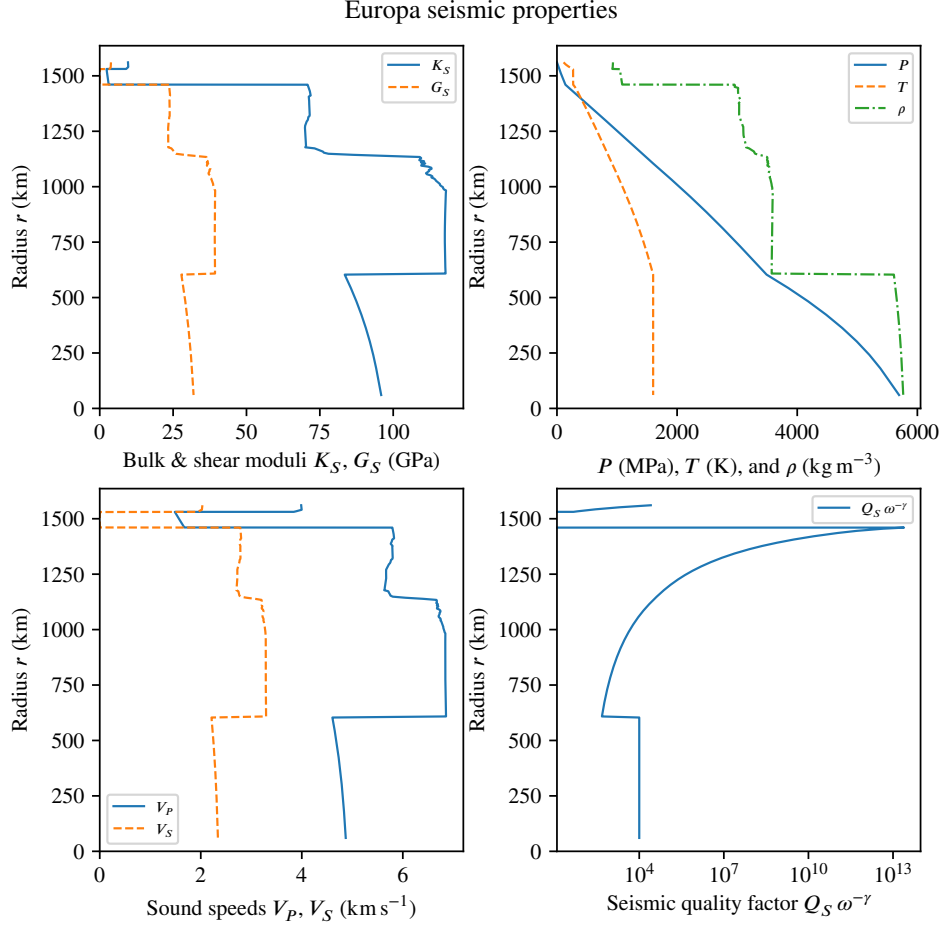


**Figure 2.** Example output figure from *PlanetProfile* containing seismic properties, including sound speeds  $V_P$  and  $V_S$ , pressure  $P$ , temperature  $T$ , density  $\rho$ , bulk and shear moduli  $K_S$  and  $G_S$ , and seismic quality factor  $Q_S \omega^{-\gamma}$ . The input model for Europa is the default listed in Table 10, with outputs detailed in Table 6 and Figure 6.

Figure 1 shows the basic organization of the self-consistent model calculations. Except for bodies like Io lacking surface water, the hydrosphere is calculated first. For the hydrosphere, the first step is to determine the pressure consistent with the assumed melting temperature, ocean composition, and salinity from laboratory EOS measurements. The properties of the ice shell are next calculated by first assuming a conductive thermal profile with no internal heating, then recalculated if convection is expected based on the Rayleigh number  $Ra$ . An adiabatic thermal profile is assumed within the ocean. Properties of rock and possible core layers are then calculated together, starting from each hydrosphere layer in turn and with core radius scaled to match the total body mass. When a core is not modeled, the rock properties are calculated for a range of porosities, retaining the mass-matching rock profile for each. Lastly, the overall profile with a calculated MoI nearest to the input MoI is selected, with seismic and electrical properties calculated for the full profile. If no calculated MoI lies within the uncertainty of the input MoI, the input configuration is deemed invalid. An example output showing several relevant properties for a profile of Europa is shown in Figure 2.

## 2.1 Ice Layers

The properties of surface ice layers are primarily set by the assumed bottom temperature  $T_b$ . At the surface is typically ice Ih, although methane clathrate may also be assumed to be present (Section 2.1.4). For thick ice shells on larger bodies like Ganymede, the pressures at the bottom of the surface ice Ih layer may be consistent with ice III (Section 2.1.3). Calculations are thus initiated by querying the ocean EOS (see Table 1) for the phase expected for the input  $T_b$  over a range of pressures above the surface pressure  $P_{\text{surf}}$ . The bottom pressure  $P_b$  consistent with the phase transition from ice Ih to another phase (liquid or ice III) is used to set the initial ice profile.

### 2.1.1 Initial Ice Shell Thermal Profile

To start, the ice shell properties are calculated from the ice Ih EOS implemented by *SeaFreeze* assuming a conductive thermal profile with the Fourier heat law (Turcotte & Schubert, 2002):

$$q = -k \frac{\partial T}{\partial r}, \quad (1)$$

where  $q$  is the upward heat flux passing through a spherical surface at radius  $r$  and  $k$  is the thermal conductivity at that surface. The thermal conductivity of ice layers is assumed to follow a  $k \sim 1/T$  dependence (Andersson & Inaba, 2005). If we further assume  $q$ , local gravitational acceleration  $g$ , and layer mass density  $\rho$  are approximately constant throughout the ice shell, Equation 1 can be manipulated to obtain

$$T(P) = T_{\text{bot}}^{\frac{P - P_{\text{top}}}{P_{\text{bot}} - P_{\text{top}}}} T_{\text{top}}^{\frac{P_{\text{bot}} - P}{P_{\text{bot}} - P_{\text{top}}}}. \quad (2)$$

In Equation 2, subscript “bot” and “top” refer to pressures  $P$  and temperatures  $T$  at the bottom and top of the ice shell, respectively. Although use of this relation represents a departure from self-consistency, as we later determine  $\rho$  and  $g$  as a function of depth, the differences will be slight except in very thick shells, where convection is expected. In those cases, the thermal profile is reassigned to account for convection (Section 2.1.2), and the properties are recalculated from the ice EOS.

The material layer is next divided into a set number of layers  $n_{\text{iceIh}}$  with a linear step in pressure, from  $P_{\text{surf}}$  to  $P_b$ , and the temperatures are assigned as in Equation 2. The physical properties (mass density  $\rho$ , heat capacity at constant pressure  $C_P$ , thermal expansivity  $\alpha$ ) are then calculated from the ice EOS using *SeaFreeze*. Finally, the thickness  $\Delta z = z_i - z_{i-1}$  of each ( $i^{\text{th}}$ ) layer is calculated, propagating downward from the surface, with

$$z_i = z_{i-1} + \frac{P_i - P_{i-1}}{g_{i-1} \rho_{i-1}}, \quad (3)$$

$$g_{i-1} = \frac{G(M - m_{\text{above}})}{r_i^2}, \quad (4)$$

where  $G$  is the gravitation constant,  $M$  is the total body mass, and  $m_{\text{above}}$  is the sum of layer masses above layer  $i$  as determined from each layer’s radius and density, resulting in  $z_b = z_{n_{\text{iceIh}}}$ . Equation 4 follows from Gauss’s law and Equation 3 follows from the local approximation  $\Delta P = \rho g \Delta z$ .

### 2.1.2 Ice Shell Convection

Once the physical properties have been calculated from the conductive profile in the ice, the Rayleigh number  $Ra$  and critical Rayleigh number  $Ra_{\text{crit}}$  can be calculated to assess whether solid-state convection is expected. The parameterization for ice shell convection implemented in *PlanetProfile* is that of Deschamps and Sotin (2001). These authors defined scaling laws for the thermal profile of convecting ice layers based on 2D

thermodynamics simulations. When the calculated Rayleigh number is greater than the critical Rayleigh number, the thermal profile is reassigned according to the scaling laws from Deschamps and Sotin (2001), with a thin lower thermal boundary layer (TBL), nearly isothermal convecting region, and conductive lid. The relevant quantities are calculated from the following relations (after Deschamps & Sotin, 2001):

$$Ra = \frac{\alpha C_P \rho g (T_b - T_{\text{top}}) z_b^3}{\eta_{\text{conv}} k} \quad (5)$$

$$\eta(T) = \eta_{\text{melt}} \exp \left\{ A \left( \frac{T_{\text{melt}}}{T} - 1 \right) \right\}, \quad (6)$$

$$T_{\text{conv}} = B \left( \sqrt{1 + \frac{2}{B} (T_b - C)} - 1 \right), \quad (7)$$

$$A = \frac{E_{\text{act}}}{RT_b}, \quad B = \frac{E_{\text{act}}}{2Rc_1}, \quad C = c_2(T_b - T_{\text{top}}), \quad c_1 = 1.43, \quad c_2 = -0.03,$$

with  $T_{\text{conv}}$  the temperature at the top of the convecting region,  $\alpha$  the thermal expansivity,  $C_P$  the heat capacity at constant pressure,  $\rho$  the mass density,  $g$  the acceleration due to gravity,  $\eta_{\text{conv}} = \eta(T_{\text{conv}})$  the viscosity at the convecting temperature,  $R$  the ideal gas constant,  $E_{\text{act}}$  the activation energy for diffusion, and  $c_1, c_2$  are fit parameters from the results of Deschamps and Sotin (2001). All quantities are in SI units (temperatures in K) except  $E_{\text{act}}$ , which is in J/mol, and  $R$ , which is in J/mol/K. The critical Rayleigh number  $Ra_{\text{crit}}$  is calculated using (Solomatov, 1995; Hammond et al., 2016)

$$Ra_{\text{crit}} = 20.9 \left( \frac{E_{\text{act}}(T_b - T_{\text{top}})}{RT_{\text{conv}}^2} \right)^4. \quad (8)$$

The Rayleigh number is defined for a region with uniform physical properties. In *PlanetProfile*, except where top or bottom values are specified, we evaluate physical properties at the midpoint in pressure  $((P_{\text{surf}} + P_b)/2)$  and at the convecting temperature after Solomatov (1995).

The method of Deschamps and Sotin (2001) prescribes layer thicknesses for the conductive lid and lower TBL based on the quantities in Equations 5–7. If the sum of these thicknesses exceeds the ice shell thickness  $z_b$  evaluated with the conductive profile, convection is assumed to be absent. Otherwise, a conductive profile is assigned to these upper and lower layers using Equation 2 and an adiabatic thermal profile is assigned to the convecting region using the procedure detailed for the ocean layers with Equation 9 (see Section 2.2).

Last, the heat flux through the ice shell is determined from the temperature difference across the lower TBL and the thermal conductivity in the convecting region us-



ing Equation 1. For shells where convection is not modeled or not occurring, the heat flux is determined using the temperature difference and thermal conductivity across the bottom ice layer. Tidal heating is not currently implemented in the ice shell, so this heat flux value is multiplied by the area of a sphere with radius  $r = R - z_b$  to get the total rate of heat loss upward through the ice shell. This value is later scaled to the heat flux from the rock layers into the hydrosphere by dividing by the surface area of a sphere with the radius at that location (Section 2.3), and also to derive the heat flux at the surface  $q_{\text{surf}}$  using the surface radius  $R$ .

### 2.1.3 Ice III, V Underplate

For cold, thick ice shells, ice III and even ice V may be present between the surface ice Ih and liquid ocean. Ice V is stable at higher pressures (above 350 MPa) than ice III (above 209 MPa), so underplating ice V is assumed to only co-occur with ice III. Such underplate layers, in direct contact with the surface ice shell, must be toggled on manually and require additional input parameters  $T_{b,\text{III}}$  and  $T_{b,\text{V}}$  to be assumed. The assumed values of  $T_{b,\text{III}}$  and  $T_{b,\text{V}}$  must be consistent with the phase diagram for each material. The properties of ice III and V underplate layers are evaluated as with ice Ih, by first supposing an initial conductive profile from Equation 2, then checking for convection using the parameterization described in Section 2.1.2. A benefit of this parameterization is that the required inputs are sufficiently general as to apply to a wide range of viscous materials for which the activation energy can be measured or estimated.

### 2.1.4 Methane Clathrates

Methane clathrate hydrates (often simply called “clathrates”) may play an important role in determining the properties of ice shells for several bodies (Mousis et al., 2015), especially Titan (Choukroun et al., 2010) and Pluto (Kamata et al., 2019), due to their high rigidity and low thermal conductivity compared to ice Ih, and their expected presence among high-volatile-content bodies. Their properties make them somewhat difficult to model self-consistently. To allow for modeling different possible configurations, three options are implemented in *PlanetProfile* for including clathrates in the ice shell: (1) conductive lid, (2) whole shell, (3) underplate. In each case, where clathrates are present they are assumed to replace ice Ih for the purpose of determining layer properties. Stability of clathrates is assessed by a common dissociation curve, based on the data pre-

sented by Choukroun et al. (2010), originally from Sloan (1998). For calculations, clathrates are divided into a number of discrete layers  $n_{\text{clath}}$ .

**In the conductive lid model,** clathrates are assumed to occupy an initial maximum thickness at the surface, which can be reduced if the dissociation temperature is exceeded along the conductive profile. After the conductive profile is evaluated, the Rayleigh number and critical Rayleigh number are calculated as with an ice Ih shell. If convection is expected, the clathrate phase is restricted to the conductive lid portion, such that clathrates extend from the surface down to the convecting portion or the input maximum depth or the point at which the dissociation temperature is exceeded, whichever is least.

**In the whole-shell clathrate model,** the dissociation curve is used to determine the ice shell bottom pressure based on the input  $T_b$ . Clathrate shell properties are then assessed using an initial conductive profile, then checked for convection as in standard ice Ih models.

**In the underplate model,** a surface heat flux  $q_{\text{surf}}$  must be assumed. This heat flux is scaled to the approximate radius of the bottom of the ice shell, then used to calculate the clathrate underplate layer thickness from the approximate thermal conductivity and the Fourier heat law (Equation 1). Because clathrate thermal conductivity is very low, most of the temperature difference across the ice shell will be across the clathrates for realistic heat fluxes for present-day icy bodies. Therefore, in this model the ice shell is assumed to be entirely conductive because the temperature difference across the overlying ice Ih layer will be too small to drive convection.

## 2.2 Ocean Layers

Within ocean layers, thermal energy is assumed to be transported efficiently by convection. On average, this results in a radial thermal profile that is adiabatic, *i.e.*, (Staley, 1970)

$$\frac{\partial T}{\partial P} = \frac{\alpha T}{\rho C_P}. \quad (9)$$

Unlike in the ice shell, ocean layer properties are calculated one layer at a time, with a linear pressure step  $\Delta P_{\text{ocean}}$  that is an input variable. The size of  $\Delta P_{\text{ocean}}$  sets the resolution of the ocean layer profile. At each step, starting from  $P_b$ ,  $T_b$  at the bottom of

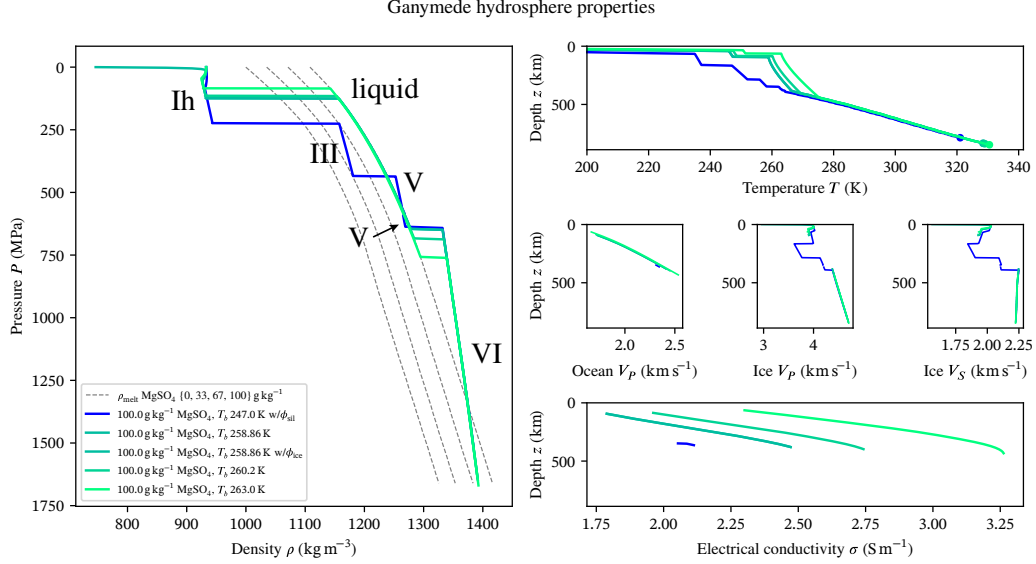


**Figure 3.** Plots of density vs. pressure and temperature, electrical conductivity, and sound speeds vs. depth for the hydrosphere of several models of Ganymede. Each model has an ocean with  $100 \text{ g kg}^{-1} \text{ MgSO}_4(\text{aq})$ . Reference curves are plotted for densities at the pressure-dependent melting temperature for 0, 33, 67, and  $100 \text{ g kg}^{-1} \text{ MgSO}_4$ . The various liquid and ice phases can be identified by jumps in the density curve. One model (blue) includes underplate ice III and V, and contains a very thin ocean because the input melting temperature is near the ice Ih–ice III–liquid triple point. This model (blue) also includes porosity modeled in rock layers (not shown; Section 2.4). A different model includes porosity modeled in ice layers (“w/ $\phi_{\text{ice}}$ ”), and exhibits a large density gradient near the surface that reflects the closure of pores due to overburden pressure.

the ice shell, the appropriate EOS for the assumed ocean solute and salinity (Table 1) is used to determine the expected phase (liquid or an ice phase). If the phase for the next  $P_i$ ,  $T_i$  layer is liquid, the physical properties  $\rho_i$ ,  $C_{P,i}$ ,  $\alpha_i$  are determined from the EOS and the next temperature  $T_{i+1} = T_i + \Delta T$  is calculated using Equation 9:

$$T_{i+1} = T_i + \Delta P_{\text{ocean}} \frac{\alpha_i T_i}{\rho_i C_{P,i}}. \quad (10)$$

If the next layer is a high-pressure (HP) phase of ice, it is assumed to be undergoing vigorous two-phase convection with the ocean fluid, such that the thermal profile is set by the pressure-dependent melting temperature. This results in a steeper temperature gradient than in the liquid layers, as demonstrated in the Ganymede hydrosphere profiles displayed in Figure 3. The melting temperature for these undersea HP ices is evaluated using the EOS in the reverse of the procedure used to find  $P_b$  from  $T_b$  at the base of the ice shell (Section 2.1)—the EOS is queried with a fixed  $P_{i+1}$  for the minimum  $T_{i+1}$  at which there is a liquid phase transition. Physical properties are then determined for the appropriate ice phase EOS using *SeaFreeze*.

Because the density of some ocean liquids can be greater above the melting point, the thermal expansivity  $\alpha$  can be negative for such liquids, creating a stably stratified layer that conducts heat rather than convecting it (Melosh et al., 2004). To account for this effect, if  $\alpha < 0$  at the top of the ocean, a conductive thermal profile is assumed, with the thermal gradient set by the heat flux  $q_b$  through the ice shell and the thermal conductivity  $k$  of water (assumed to be  $0.55 \text{ W m}^{-1} \text{ K}^{-1}$ ) and the Fourier heat law (Equation 1). The physical properties are evaluated step-by-step as in the convecting case, but using a smaller pressure step for the conductive layer, which is expected to be only  $\lesssim 200 \text{ m}$  thick (Melosh et al., 2004). This process is continued until  $\alpha > 0$  or a phase change is reached, at which point the phase-dependent approach described above is applied. Future development plans include a self-consistent calculation of thermal conductivity for all materials (Section 2.7); currently only ice Ih has such a calculation in *PlanetProfile*.

In all cases, calculation of the physical properties with each layer from  $P_i$  and  $T_i$  also permits a determination of layer thickness using Equations 3 and 4. This process is repeated until an arbitrary threshold pressure  $P_{\text{hydro,max}}$  is reached, which is set as an input. Each hydrosphere layer radius  $r_i$  is used as a starting point for possible sizes of the rock/core layers, to provide multiple options for finding a fit to the measured MoI. Therefore,  $P_{\text{hydro,max}}$  must be greater than the expected pressure at the hydrosphere—

rock transition depth.  $P_{\text{hydro,max}}$  is intended to be set as low as possible to limit excess computation time. However, if  $P_{\text{hydro,max}}$  is set too low, possible sizes of rock+core layers that best match the measured MoI may be excluded from the search space, resulting in an invalid profile or one that is skewed toward one end of the MoI uncertainty bounds.

### 2.3 Rock and Metallic Core Layers

In order to match the total body mass and MoI self-consistently, the inner layers (those of rocks and possible core) must have their properties determined all the way to the body center for multiple starting sizes. This is because the density of the material at each layer depends on the overburden pressure and the temperature. A warmer profile will have less dense materials, requiring a larger radius for inner layers to match the total body mass, increasing those outer layers' contribution to the MoI. Conversely, a colder profile will concentrate greater densities at deeper layers within the body, resulting in a smaller MoI. Furthermore, the total heat leaving the rock portion is assumed to be equal to that escaping through the ice shell, because the ocean is assumed to convect the heat generated in the interior instantaneously on geologic timescales. This adds a dependence on the hydrosphere layer profile to the thermal profiles modeled in the inner layers. For waterless bodies, the surface heat flux is an input quantity and variation for matching the MoI is achieved by varying the porosity.

In both rock and core layers, physical properties are evaluated by interpolating  $P$ - $T$  EOS data tables generated by *Perple-X* (Connolly, 2009). The *Perple-X* software calculates physical properties of mineral assemblages based on an input chemical composition by Gibbs free energy minimization. For rocks, we have generated lookup tables for chemical compositions over  $P$  and  $T$  conditions relevant to solar system moons based on chondritic and cometary material that has partially differentiated, such that free fluids have been lost to the ocean or to space, but volatile-bearing and volatile-free minerals, dense iron, and siderophile elements are retained. In the current version of *PlanetProfile*, only solid phases are modeled, although implementing self-consistent melt for rock and metallic layers is in progress (Section 2.7).

Chondrite types CI, CM, and CV are included (elemental composition from Lodders and Fegley (1998) and Lodders (2021)), as is a composition consistent with Comet 67P/C-G (based on combining: Filacchione et al. (2019); Bardyn et al. (2017); Le Roy et al. (2015);

Pätzold et al. (2016); Dhooghe et al. (2017)). Additionally, for CM chondrites, we include a fully differentiated composition relevant to Ganymede based on an estimated metallic core size and an input sulfur sequestration, from 0 wt% S to 20 wt% S in the core. The maximum of these is the approximate total sulfur that a bulk-CM-chondrite Ganymede could lose to the core if the primordial sulfur content were all sequestered in the core.

In rock layers, a conductive thermal profile is assumed. This is not a good approximation for bodies like Io, where the surface heat flux can be over  $2 \text{ W m}^{-2}$  (Lainey et al., 2009). However, MoI-matching density profiles for rocks may be found for heat fluxes about 10% of this rate. An implementation for self-consistent convection modeling in rocks is being developed (Section 2.7). Application to Io is discussed further in Section 4.

For the conductive thermal profile in rocks, the Fourier heat law can be integrated to obtain an expression accounting for internal heating (Turcotte & Schubert, 2002):

$$T_{\text{bot}} = T_{\text{top}} + \frac{H_{\text{tot}}}{6k} (r_{\text{top}}^2 - r_{\text{bot}}^2) + \left( \frac{q_{\text{top}} r_{\text{top}}^2}{2k} - \frac{H_{\text{tot}} r_{\text{top}}^3}{6k} \right) \left( \frac{1}{r_{\text{bot}}} - \frac{1}{r_{\text{top}}} \right), \quad (11)$$

$$H_{\text{tot}} = H_{\text{tidal}} + \rho_{\text{rad}} Q_{\text{rad}},$$

where  $T_{\text{bot}}$ ,  $T_{\text{top}}$ ,  $r_{\text{bot}}$ ,  $r_{\text{top}}$  are the temperatures and radii at the bottom and top of the discrete layer,  $k$  is thermal conductivity,  $q_{\text{top}}$  is the heat flux leaving the top surface of the layer,  $H_{\text{tidal}}$  is the volumetric heating (from tidal forces) in  $\text{W m}^{-3}$ ,  $\rho_{\text{rad}}$  is the density of materials contributing radiogenic heating, and  $Q_{\text{rad}}$  is the radiogenic heating rate in  $\text{W kg}^{-1}$ . All quantities are in SI units. In *PlanetProfile*, fixed tidal heating and radiogenic heating rates are assumed as inputs. Self-consistent calculation of tidal heating rates throughout the interior is in development, using a Python adaptation of the *ALMA3* package (Spada, 2008), *PyALMA* (Section 2.7).

Rock layer properties are evaluated all the way from each starting hydrosphere layer radius down to the center of the body. To save on computational overhead, the default behavior is to begin this profile search starting from each ocean layer. If a mass-matching profile is not found, the profile search is restarted from the surface to account for bodies that may be fully frozen. A fixed number of layers  $n_{\text{sil}}$  sets the profile resolution in this region, and a linear step in radius is now used. Many of these hydrosphere+rock profiles will exceed the body mass; those that do are immediately discarded. For the remaining profiles, the method of matching the MoI varies depending on whether or not a core is intended to be modeled. When no core is modeled, the profile with greatest mass that

is less than the total body mass is retained as a candidate for MoI matching, the vacuum porosity  $\phi_{\text{rock}}$  is increased, and the process is repeated for  $n_\phi$  total profiles over a range of  $\phi_{\text{rock}}$  values.

### 2.3.1 *Metallic Core Layers*

When a core is modeled, the core layers are handled last as they are at the center of the body. As described above, physical properties of core layers are evaluated by interpolating *Perple\_X* data tables using the thermodynamic data of Saxena and Eriksson (2015). We have generated *Perple\_X* tables for core compositions ranging from pure iron (100 wt% Fe) to the maximum core sulfur content of  $\sim 35$  wt% S (100 wt% FeS) in 5 wt% S increments, resulting in a single 3D data table in  $P$ - $T$ - $x_{\text{FeS}}$ . This 3D table is interpolated based on an input core sulfur mixing ratio  $x_{\text{FeS}}$  to obtain a  $P$ - $T$  EOS for the core material.

The core layers must now be evaluated. First, a maximum core size is set based on a minimum density  $\rho_{\text{core,min}}$  below that expected (*e.g.*,  $4500 \text{ kg m}^{-3}$ , the density of FeS at  $\sim 2.6$  GPa and 1350 K). The maximum core size is that consistent with an amount of innermost rock layers replaced by core material with a density  $\rho_{\text{core,min}}$ , such that the total mass is just less than the measured body mass. Similar to starting the rock profile search from each ocean layer by default, this maximum core size is used to reduce computational overhead, by reducing the number of core profiles to iterate over.

Next, the rock layers with outer boundaries inside the maximum core radius are each used as a starting point for the core layer profiles. A linear step in radius is used, and for a fixed number of layers  $n_{\text{core}}$  the thermal profile is assumed to be adiabatic (Equation 9). Physical properties are calculated from the top down, one core layer at a time, starting from the pressure, temperature, and local gravity at the top of the first rock layer replaced. The local gravity for each core layer is modeled as proportional to radius, which is only true for a constant density sphere, but the density typically changes very little across core layers because of the adiabatic assumption. The core profile search operation is performed in a vectorized fashion across each rock profile. Finally, the single core profile for each rock profile that is the greatest mass less than the total body mass is selected as the best fit. This gives a set of mass-matching core+rock profiles, from among which the best-fit MoI is selected as the model output (Section 2.3.2).

A toggle is included to skip the self-consistent rock layer calculation, and instead use a uniform density for both rocks and core. In this case, the core density is assumed as an input and the core size is scaled to match the total body mass. This option is included to match the behavior of previous versions of the software (*e.g.*, Vance et al., 2018) and for faster operation in large parameter-space searches.

For bodies like Io where no surface water is modeled, there is only one radius available for the rock profile search. Whether a core is modeled or not, the rock vacuum porosity  $\phi_{\text{rock}}$  is varied over an input range as in the case where no core is modeled. When a core is modeled, the core profile search algorithm is the same as for models with a hydrosphere—only the mass-matching rock+core profile for each value of  $\phi_{\text{rock}}$  is carried forward to the MoI-matching calculation.

### 2.3.2 Matching the MoI

Once the set of mass-matching, full-body profiles has been generated, they are each compared to the MoI to determine which best matches. As the profiles are spherically symmetric, each layer’s contribution to the total axial moment of inertia  $C$  is

$$\Delta C_i = \frac{8\pi}{15} \rho_i (r_i^5 - r_{i+1}^5), \quad (12)$$

with the final radius  $r_{n_{\text{tot}}+1} = 0$  at the center of the body and  $C = \sum \Delta C_i$ . This expression follows from the uniform-density layers in our model and the moment of inertia definition (*e.g.*, Morin, 2008)

$$C = \int_M s^2 dm, \quad (13)$$

where  $s$  is the distance between each  $dm$  and the axis of rotation associated with  $C$ .

The profile with the MoI closest to the measured value is highlighted as the best match to the inputs and assumptions. Several bulk properties are calculated at this stage, such as the mean rock density, thickness of the ocean layer, total mass of dissolved salts, *etc.* Several of these properties are compared among the other profiles that fit within the input uncertainty for the MoI in order to estimate the range of uncertainty in these quantities. The individual layer properties for only the best-match profile are retained for the final processing steps and for saving to disk.



## 2.4 Porosity in Rock and Ice Layers

*PlanetProfile* supports modeling of porosity in rock and ice layers (independent of one another). These features can optionally be enabled for any model, and porosity in rock layers is required for self-consistent modeling of bodies with no metallic core or hydrosphere. Porosity in any material follows the same general framework (Han et al., 2014):

$$\phi(P) = \phi_{\text{vac}} \exp \left\{ -\frac{cP}{P_c} \right\}, \quad (14)$$

where  $\phi(P)$  is the volume fraction of void space within the matrix as a function of pressure,  $\phi_{\text{vac}}$  is the porosity of the material if there were no overburden pressure (extrapolated for materials like ice III that are not stable at low pressures),  $c$  is a constant (6.15), and  $P_c$  is an experimentally derived pore closure pressure, beyond which pores are effectively eliminated ( $\phi < 0.2\%$ ).

Based on other characteristics of the model, the pore space is assumed to be evacuated or filled with other materials. In ices near the surface, and in rocks for bodies with no hydrosphere, pores are assumed to be evacuated. Within HP ices found within ocean fluids, the pore space is assumed to be filled with ocean fluid. Because these layers are assumed to be at the melting temperature, both ice and fluid are stable and the ocean EOS is used to determine pore fluid properties. Within porous rocks beneath a hydrosphere, the pores are assumed to be filled with ocean fluids, and the ocean EOS and pore-space  $P$  and  $T$  conditions are used to determine the phase and properties of the pore material. Pore materials are assumed to have the same temperature as the matrix in which they are embedded.

When the pore material is liquid, the matrix material is assumed to rigidly support the overburden pressure, such that the pore space pressure increases based on the local gravity and the overburden pressure of only the pore material. Pore spaces are assumed to be sufficiently permeable as to communicate these pressures vertically. The pore pressure is assumed to provide a counteracting force that acts to hold pores open, ultimately resulting in a net effective pressure  $P_{\text{eff}}$  in Equation 14 that determines the porosity (Vitovtova et al., 2014):

$$P_{\text{eff}} = P_m - \alpha_{\text{eff}} P_f, \quad (15)$$

where  $P_m$  is the overburden pressure for the matrix material,  $P_f$  is the pressure within the pore fluid, and  $\alpha_{\text{eff}}$  is a constant that characterizes the behavior of the matrix. In *PlanetProfile*,  $\alpha_{\text{eff}}$  is a variable, by default set to 0.95 after Vitovtova et al. (2014).

Physical properties of the pore and matrix materials are combined to get bulk layer properties using the two-phase composite model of Yu et al. (2016):

$$M^J = (1 - \phi)M_f^J + \phi M_m^J, \quad (16)$$

where  $M_m$  and  $M_f$  stand for a mechanical property for the matrix and pore fluid respectively,  $M$  is the same mechanical property for the combined two-phase layer, and  $J$  is a mixing parameter that depends on the character of pores and the mechanical property. Considering two-phase porous materials,  $J$  typically ranges from 0 to 1, and can be greater than 1 for seismic velocities in some materials (Yu et al., 2016). For several properties, such as density  $\rho$ ,  $J = 1$  and Equation 16 describes an arithmetic mean, weighted by  $\phi$ . In *PlanetProfile*, a  $J$  value for each layer property is set independently, for porous rock and ice separately; we assume  $J = 1$  for all properties except the seismic properties:

Bulk modulus:  $J_{K_S} = 0.35$

Shear modulus:  $J_{G_S} = 0.35$

P-wave speed:  $J_{V_P} = 0.75$

S-wave speed:  $J_{V_S} = 0.85$ .

These values are selected as rough “middle” estimates from the mineral assemblages studied by Yu et al. (2016). If these values are known for a specific assumed mantle composition, each  $J$  should be updated to the known value for self-consistency.

## 2.5 Seismic and Electrical Properties

Seismic and electrical properties for each layer profile are calculated from  $P$ ,  $T$ , and  $\phi$  conditions for each layer after the entire self-consistent physical structure has been determined. Seismic properties are determined from the EOS (Table 1); for some materials, such as methane clathrates, the  $P$ – $T$  dependence of the seismic properties is implemented separately from other physical properties. Output files formatted for compatibility with the open-source packages *AxiSEM* (Nissen-Meyer et al., 2014) and *Mineos* (<https://github.com/geodynamics/mineos>) are printed at the end of each model run. Past studies (*e.g.*, Stähler et al., 2018) have paired previous versions of *PlanetProfile* with *AxiSEM* to understand how seismic data may aid in constraining the interior structure of icy moons. The *TauP* package (Crotwell et al., 1999) implemented in the open-source

*ObsPy* framework (Beyreuther et al., 2010) provides complementary calculations for seismic travel times; integration with this package is a work-in-progress. Calculated seismic and physical properties can also be passed to gravitational modeling software such as *ALMA3* (Section 2.7), for example in iterative modeling that evaluates tidal heating self-consistently.

Depth-dependent electrical properties are critical for magnetic sounding investigations that connect magnetic measurements to interior structure (Vance et al., 2021). On global scales, conductivity of ice ( $\sim 10^{-5} \text{ S m}^{-1}$ , Petrenko & Schulson, 1992), clathrate ( $\sim 10^{-5} \text{ S m}^{-1}$ , Stern et al., 2021), and rock matrix materials ( $\lesssim 10^{-7} \text{ S m}^{-1}$ , Glover & Vine, 1994) are expected to be negligible for the hours-long oscillations of planetary magnetic fields. In *PlanetProfile*, we set the conductivity of many of these materials to an arbitrarily small value ( $10^{-8} \text{ S m}^{-1}$ ). Metallic core layers are expected to have a high conductivity ( $\sim 10^6 \text{ S m}^{-1}$ , Pozzo et al., 2012), so we set them to an arbitrarily large value ( $10^6 \text{ S m}^{-1}$ ).

For the ocean and pore-filling fluids, electrical conductivity is determined from empirical models, interpolation, and/or extrapolation of available laboratory measurements (Table 1). Pure water conductivity is set to a constant  $\sigma = 10^{-5} \text{ S m}^{-1}$  (Light et al., 2004), as even dilute ions will dominate the electrical properties (*e.g.*, Quist & Marshall, 1968) and pure water oceans will probably not persist over geologic time scales as materials dissolve into the fluid. Seawater conductivity is determined as a function of  $P$ ,  $T$ , and salinity  $w$  using the Python implementation of the *Gibbs Seawater* package (McDougall & Barker, 2011). Following Vance et al. (2018), conductivity of  $\text{MgSO}_4(\text{aq})$  ocean fluids is determined by interpolation of measurements at relevant conditions from Larionov and Kryukov (1984). The laboratory measurements these implementations are based on were necessarily limited. For  $\text{MgSO}_4$  oceans, the data are extrapolated above  $1.2 \text{ g kg}^{-1}$ , below 298 K, and above 784 MPa. This extrapolation is justified by smooth functional behavior and the expected physical dependence (Vance et al., 2018). The need for extrapolation underscores the critical importance of future laboratory measurements of electrical conductivities for solutions at  $P$  and  $T$  conditions that are relevant to ocean worlds.

## 2.6 Magnetic Induction Properties

To determine properties of the induced magnetic field from each body, *PlanetProfile* makes use of the open-source Python framework *MoonMag* (Styczinski, Vance, Harnett, & Cochrane, 2022). *MoonMag* calculates induced magnetic fields from a description of the excitation moments, the radial conductivity profile, and the shape of asymmetric conducting boundaries in terms of spherical harmonic coefficients. Excitation moments are the amplitudes, phases, and periods of oscillation for each vector component of the time-varying magnetic field applied to the body. The excitation moments must be estimated or determined from planetary magnetospheric models. *PlanetProfile* uses excitation moments calculated using Fourier methods (Vance et al., 2021). SPICE kernels are used to evaluate the moons' locations and planet orientation. Combined with planetary field models detailed in the literature, the magnetic field is evaluated at the body in a time series that is inverted to obtain the excitation moments.

The induced field is determined by a recursive layer method (Styczinski, Vance, Harnett, & Cochrane, 2022), where each layer has uniform conductivity. The time required to calculate the induced field is linear in the number of conducting layers for symmetric models, so the conductivity profile is contracted before being passed to *MoonMag*. All adjacent layers with conductivity below or above threshold values are combined into a single low- or high- conductivity layer. Layers such as those in the ocean with conductivities between this range may optionally be reduced to a fixed number of interpolated layers (default 5). The depth dependence of conductivity within ocean layers has significant effects on the induced magnetic moments (Vance et al., 2021); we consider this approach to be an acceptable compromise between uniformly conducting oceans and those with excessively high spatial resolution, given other model uncertainties and approximations.

*MoonMag*, and its implementation within *PlanetProfile*, also supports asymmetric boundary shapes. All large moons in the solar system rotate synchronously, so each has substantial  $J_2$  and  $C_{22}$  gravity coefficients, describing oblateness and elongation, respectively. Therefore, some asymmetric shape is expected from orbital motion and gravity alone. For most moons, the gravity coefficients contribute half or more of the expected difference from asymmetric layers (Styczinski, Vance, Harnett, & Cochrane, 2022). Asymmetric models can add substantial computation time, so for most bodies only gravity co-

efficients are considered. For some bodies, such as Enceladus, the ocean is known to have an asymmetric interface with the ice shell (Hemingway & Mittal, 2019); for such bodies, the induced field is significantly affected and example asymmetric shapes are included with the default model (Section 3).

Several helpful features are wrapped from or re-implemented based on *MoonMag*, including evaluating the induced magnetic field at points on the surface or along a spacecraft trajectory relative to the body. Also implemented are a number of helper functions for generating or evaluating parameter-space searches and statistical analyses. For example, functions to create “induct-o-gram” plots vary two relevant parameters affecting ocean properties such as a fixed (“silicate”) rock density  $\rho_{\text{rock}}$  and salinity  $w$  over some range for each. The induced field at the magnetic pole is then evaluated over a grid of values for each parameter and contours of the field strength are plotted (Figure 4). This has an advantage over canonical induct-o-gram plots (*e.g.*, Khurana et al., 2002) with uniform ocean conductivity  $\bar{\sigma}$  and total ocean layer thickness  $D$ , as  $\bar{\sigma}$  and  $D$  are not independent in self-consistent models. For Bayesian methods involving a parameter adjustment between each model run—*e.g.*, finding maximum likelihood for model parameters based on a fit to magnetometer data—individual model runs can be chained together with a helper function (`UpdateRun`). This function recalculates only those portions of the prior self-consistent model solution that will be affected by the desired parameter update, saving computation time.

## 2.7 Directions for Future Development

*PlanetProfile* is in active development. A number of updates are planned or in-progress that are intended to improve on the self-consistency of the models and their utility in scientific applications. Improvements in progress include:

1. Convection in rocks. Models are currently limited to conductive thermal profiles in rock layers, which will only be realistic for bodies without significant internal heating.
2. Including metallic core and rock melt fraction from *Perple\_X*. The *Perple\_X* tables currently implemented in *PlanetProfile* for the EOS for rock and core materials include only the properties of the solid matrix, even when molten rocks are present.

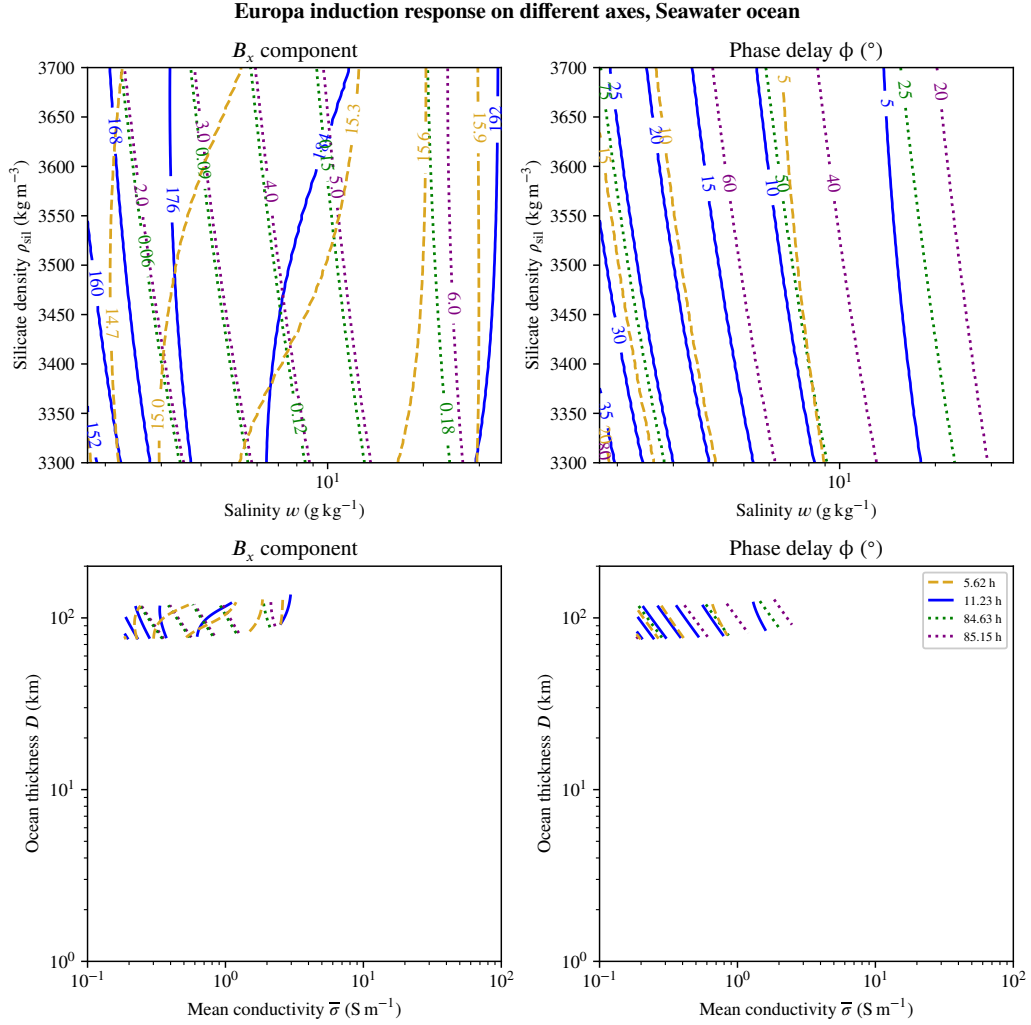


**Figure 4.** Induct-o-gram showing the induction response strength and phase delay in the  $B_x$  component for Europa (IAU coordinates) at the moving magnetic pole relative to several body properties. Model inputs are the axes on the top two panels, a fixed (“silicate”) rock density  $\rho_{\text{rock}}$  and Seawater salinity  $w$ . The bottom two panels show the same contours as the top, but plotted against the mean conductivity  $\bar{\sigma}$  and total ocean thickness  $D$  of the self-consistent models. The range of values shown for  $\bar{\sigma}$  and  $D$  is consistent with past studies (*e.g.*, Zimmer et al., 2000; Khurana et al., 2002; Vance et al., 2021), demonstrating that such a wide parameter space is likely not necessary to consider when further constraints are included.

3. Self-consistent rock layers with variable iron and sulfur differentiation. The total elemental content of a body is limited by its primordial abundances. Since we assume a chondritic or cometary origin, the iron and sulfur content in the core is dependent on how much can be extracted from the rocks, and the total budget in both sources should be consistent with the assumed parent material.
4. Self-consistent tidal heating with *PyALMA*, including iterative profile evaluation. An in-progress Python implementation of *ALMA3* (Melini et al., 2022), called *PyALMA*, supports the calculation of gravitational Love numbers from standard *PlanetProfile* output files. The tidal Love numbers  $h_2$  and  $k_2$  describe the response of a body to gravitational forcing and can be used to derive tidal heating rates, but themselves depend on the material properties. Self-consistency of *PlanetProfile* models can be improved by using *PyALMA* to calculate Love numbers following a model run, then calculating tidal heating rates from the Love numbers and using these rates as inputs to a second model iteration. This process can then be repeated until the model converges.  $h_2$  and  $k_2$  are also indirectly observable through gravity and geodetic measurements, providing additional means of constraining interior structure from *PlanetProfile* models.
5. Integration with the *TauP* package. Calculation of seismic wave travel times will provide an additional connection between interior structure model outputs and measurements available to spacecraft.

Improvements planned for the future include:

1. Self-consistent thermal profile in ice, including tidal heating and  $T_b$  values derived from surface heat flux. The initial thermal profile in the ice shell is determined from the assumed ocean melting temperature and the assumption of a  $1/T$  dependence for the ice thermal conductivity  $k$ . A more self-consistent method is desirable, and converting the assumptions required to an input surface heat flux is one way to resolve this issue.
2. Improved convection parameterization in ice. Convection in the ice shell is modeled after Deschamps and Sotin (2001). The fit parameters for this model were derived for a specific case with no tidal heating. Implementing a convection model that accounts for tidal heating would improve self-consistency.

3.  $P$ - and  $T$ -dependent calculations of  $k$  for all materials. Thermal conductivity  $k$  is calculated as a function of  $T$  only, and only for ice layers. For all other materials,  $k$  is set to a constant. Especially for conductive profiles in rock layers, this approximation limits the range of validity of the models.
4. More options for ocean fluids, as they become implemented in *SeaFreeze*. A wide variety of solutes are possible and likely to be found in subsurface oceans of icy moons. Notably absent from the EOS data currently implemented in *PlanetProfile* is ammonia ( $\text{NH}_3$ ), which is expected to be common in the outer solar system and likely contributes significantly to ocean properties (Choukroun & Grasset, 2010; Kimura & Kamata, 2020). A wider range of supported fluids is expected to be implemented in *SeaFreeze* as more laboratory measurements become available.
5. Time-dependent models. *PlanetProfile* models assume the body is in steady-state, *i.e.*, the heat flux entering and leaving each layer is equal and no melting or freezing is actively occurring. If this assumption were to be relaxed, *PlanetProfile* models could be used as a starting point for projecting forward or backward in time to study the evolution of terrestrial bodies.

### 3 Model Results Across the Outer Solar System

*PlanetProfile* is designed to be versatile in allowing for investigation of a wide variety of assumed input properties. To serve as a starting point from which to iterate, *PlanetProfile* comes packaged with a default model for each major moon in the solar system and Pluto. After the package is installed or cloned from the GitHub repository, an installation function copies default models to the working directory so they can be easily accessed and edited by the user. These models represent a synopsis of measured and estimated characteristics for each body based on the available literature and features implemented in *PlanetProfile*.

Tables 5–9 describe major layer properties calculated for each default model using *PlanetProfile*. Figures 5–9 show “wedge” diagrams representing the material layers described in the corresponding tables. These figures and tables (L<sup>A</sup>T<sub>E</sub>X source) are output directly by the software. We have grouped together the output summary tables and figures by size to show greater detail in the wedge diagrams for smaller bodies. Tables 10–13 contain the major input parameters for each model along with references to sources from the literature. Text files containing the full model outputs are available as



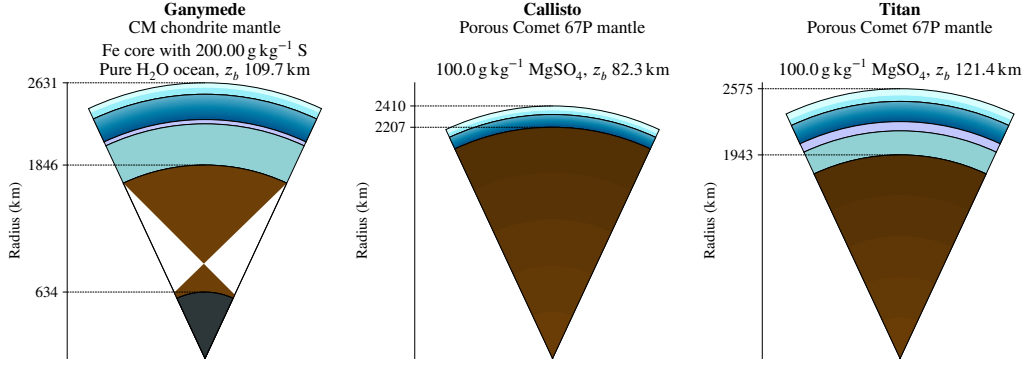


**Figure 5.** Wedge diagram showing major material layers for default models of the largest moons: Ganymede, Callisto, and Titan, to scale. The depicted models are as summarized in Table 5. Conducting ice Ih, at the surface of each body, is shown in pale blue; convecting ice Ih, which is present for all of these models, is cyan; ocean layers are blue with a color gradient; ice V is lavender; ice VI is gray-green; rock is brown, and porous rock is shown with a color gradient; metallic core layers are dark gray.

a Zenodo archive: <https://doi.org/10.5281/zenodo.7250785>. These files each list the hundreds of individual layers that make up the profile, along with the material type and physical properties. A number of header lines also describe bulk properties and selected input parameters.

## 4 Discussion

Geophysical models applied in planetary science typically either focus on large-scale material layers with uniform properties or smaller-scale, more detailed dynamical modeling that cannot easily be scaled to a global context. *PlanetProfile* represents a compromise between these extremes. Spherical symmetry allows models to be run quickly, while still capturing major global-scale processes. Application of scaling laws from more detailed studies and EOS data from laboratory measurements over many individual layers affords much greater fidelity between required assumptions and results of the model than is possible in simpler approaches. To our knowledge, the only comparable software available is *BurnMan* (Cottaar et al., 2014), but *BurnMan* focuses on Earth-like interiors and is not intended for application to icy bodies with subsurface oceans.

**Table 5.** *PlanetProfile* output summary table for default models of the largest moons:

Ganymede, Callisto, and Titan. Material layers are depicted in Figure 5.  $M$ : total body mass;  $C$ : axial moment of inertia;  $R$ : outer radius of layer;  $\rho_{\text{rock,mean}}$ : mean density of rock layers, including pore fluids;  $T_b$ : temperature at bottom of ice shell;  $q_{\text{surf}}$ : surface conductive heat flux;  $q_{\text{con}}$ : heat flux through ice shell at the bottom of the conductive layer;  $\eta_{\text{con}}$ : ice viscosity for possible convecting region based on Deschamps and Sotin (2001) approach;  $D_{\text{Ih}}$ ,  $D_{\text{V}}$ ,  $D_{\text{VI}}$ : thickness of ice layers;  $D_{\text{ocean}}$ : thickness of contiguous liquid water ocean layer;  $\bar{\sigma}_{\text{ocean}}$ : mean conductivity across contiguous ocean layers (each linear pressure step is weighted uniformly);  $\phi_{\text{rock}}$ : vacuum porosity of rocks. Upper and lower uncertainty values on  $C_{\text{model}}/MR^2$  results represent the next nearest models. A zero value indicates that no valid model lies between the best match and the uncertainty bounds of the input  $C/MR^2$  value.

	<b>Ganymede</b>	<b>Callisto</b>	<b>Titan</b>
Ocean comp.	Pure H <sub>2</sub> O	100.0 g kg <sup>-1</sup> MgSO <sub>4</sub>	100.0 g kg <sup>-1</sup> MgSO <sub>4</sub>
$M$ (kg)	$1.4819 \times 10^{23}$	$1.0759 \times 10^{23}$	$1.3452 \times 10^{23}$
$M_{\text{model}}$ (kg)	$1.4819 \times 10^{23}$	$1.0756 \times 10^{23}$	$1.3447 \times 10^{23}$
$C/MR^2$	$0.3115 \pm 0.0028$	$0.3549^{+0.0042}_{-0.0148}$	$0.341^{+0.010}_{-0.020}$
$C_{\text{model}}/MR^2$	$0.31143^{+0.00023}_{-0.00025}$	$0.34121^{+0.00000}_{-0.00000}$	$0.32143^{+0.00000}_{-0.00022}$
$\rho_{\text{rock,mean}}$ (kg m <sup>-3</sup> )	3237	2066	2795
$T_b$ (K)	258.86	262.0	255.0
$q_{\text{surf}}$ (mW m <sup>-2</sup> )	16.3	18.3	12.4
$q_{\text{con}}$ (mW m <sup>-2</sup> )	17.7	19.6	13.6
$\eta_{\text{con}}$ (Pa s)	$5.89 \times 10^{14}$	$5.35 \times 10^{14}$	$8.48 \times 10^{14}$
$D_{\text{Ih}}$ (km)	109.7	82.3	121.4
$D_{\text{ocean}}$ (km)	241.2	121.3	192.7
$D_{\text{V}}$ (km)	40.9	-	88.2
$D_{\text{VI}}$ (km)	393.2	-	229.3
$\bar{\sigma}_{\text{ocean}}$ (S m <sup>-1</sup> )	0.0	2.4	1.4
$R_{\text{surf}}$ (km)	2631.2	2410.3	2574.7
$R_{\text{rock}}$ (km)	1846.1	2206.7	1943.1
$R_{\text{core}}$ (km)	633.8	-	-
$\phi_{\text{rock}}$	-	0.90	0.90

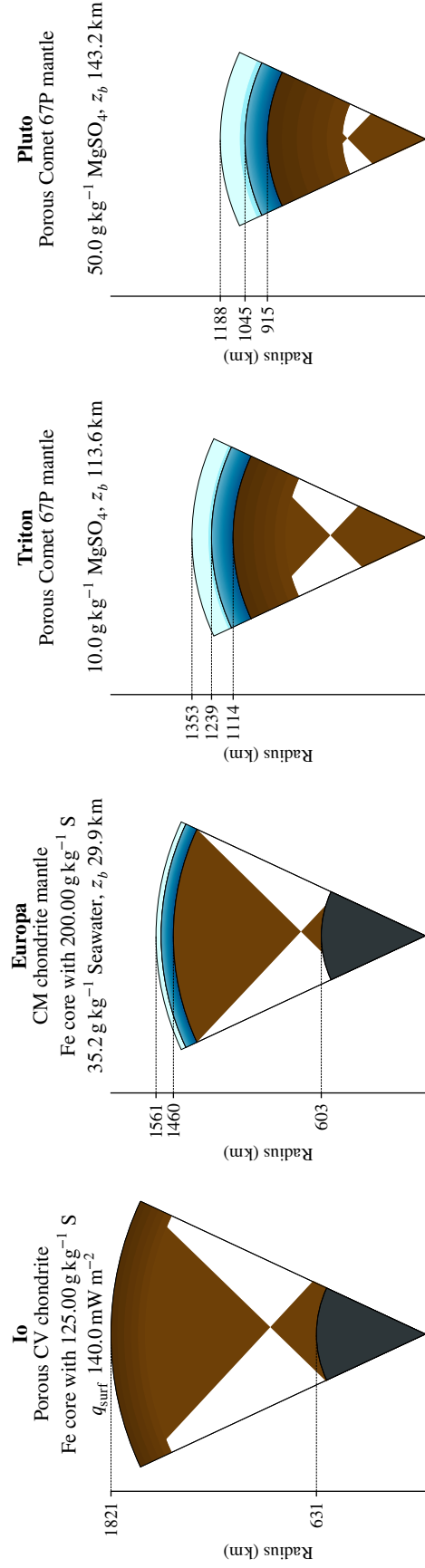


**Figure 6.** Wedge diagram showing major material layers for default models of large moons Io, Europa, and Triton with similarly-sized Pluto, to scale. The depicted models are as summarized in Table 6; layer colors are indicated as described in Figure 5.

**Table 6.** *PlanetProfile* output summary table for default models of large moons Io, Europa, and Triton with similarly-sized Pluto. Material layers are depicted in

Figure 6. Variable definitions are as in Table 5.

	<b>Io</b>	<b>Europa</b>	<b>Triton</b>	<b>Pluto</b>
Ocean comp.	No H <sub>2</sub> O	35.2 g kg <sup>-1</sup> Seawater	10.0 g kg <sup>-1</sup> MgSO <sub>4</sub>	50.0 g kg <sup>-1</sup> MgSO <sub>4</sub>
$M$ (kg)	$8.9320 \times 10^{22}$	$4.8000 \times 10^{22}$	$2.1410 \times 10^{22}$	$1.3030 \times 10^{22}$
$M_{\text{model}}$ (kg)	$8.9251 \times 10^{22}$	$4.7986 \times 10^{22}$	$2.1408 \times 10^{22}$	$1.3028 \times 10^{22}$
$C/MR^2$	$0.37685 \pm 0.00035$	$0.346 \pm 0.005$	$0.31 \pm 0.03$	$0.31 \pm 0.03$
$C_{\text{model}}/MR^2$	0.37688	$0.34593^{+0.00038}_{-0.00037}$	$0.32916^{+0.00004}_{-0.00000}$	$0.32028^{+0.00006}_{-0.00000}$
$\rho_{\text{rock,mean}}$ (kg m <sup>-3</sup> )	3404	3287	2908	2863
$T_b$ (K)	-	268.305	266.0	265.0
$q_{\text{surf}}$ (mW m <sup>-2</sup> )	140.0	16.0	11.6	9.5
$q_{\text{con}}$ (mW m <sup>-2</sup> )	-	16.7	13.8	12.2
$\eta_{\text{con}}$ (Pa s)	-	$3.49 \times 10^{14}$	$2.92 \times 10^{14}$	$3.30 \times 10^{14}$
$D_{\text{th}}$ (km)	-	29.9	113.6	143.2
$D_{\text{ocean}}$ (km)	-	70.9	125.1	129.9
$\bar{\sigma}_{\text{ocean}}$ (S m <sup>-1</sup> )	-	2.8	0.3	1.4
$R_{\text{surf}}$ (km)	1821.5	1560.8	1352.6	1188.3
$R_{\text{rock}}$ (km)	1821.5	1460.0	1113.9	915.2
$R_{\text{core}}$ (km)	631.4	603.5	-	-
$\phi_{\text{rock}}$	0.70	-	0.35	0.35

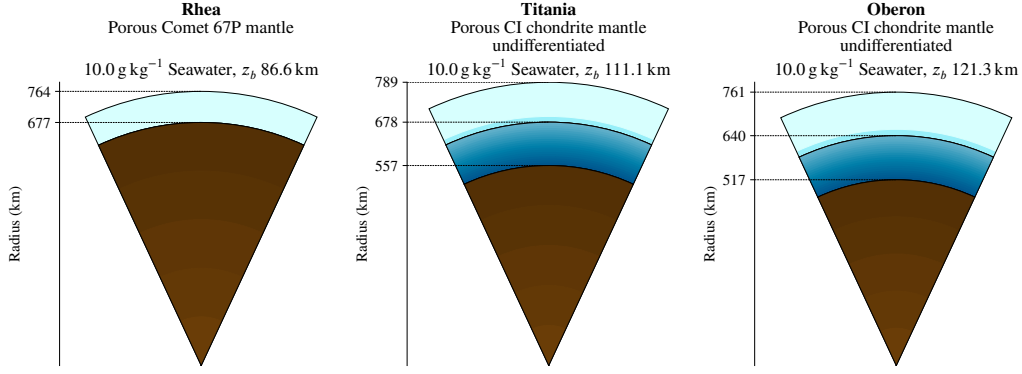


**Figure 7.** Wedge diagram showing major material layers for default models of mid-sized moons Rhea, Titania, and Oberon, to scale. The depicted models are as summarized in Table 7; layer colors are indicated as described in Figure 5.

**Table 7.** *PlanetProfile* output summary for default models of mid-sized moons Rhea, Titania, and Oberon. Material layers are depicted in Figure 7. Variable definitions are as in Table 5.

	Rhea	Titania	Oberon
Ocean comp.	10.0 g kg <sup>-1</sup> Seawater	10.0 g kg <sup>-1</sup> Seawater	10.0 g kg <sup>-1</sup> Seawater
$M$ (kg)	$2.3065 \times 10^{21}$	$3.5270 \times 10^{21}$	$3.0140 \times 10^{21}$
$M_{\text{model}}$ (kg)	$2.2994 \times 10^{21}$	$3.5260 \times 10^{21}$	$3.0103 \times 10^{21}$
$C/MR^2$	$0.3721 \pm 0.0036$	$0.306 \pm 0.03$	$0.307 \pm 0.03$
$C_{\text{model}}/MR^2$	$0.37132^{+0.00000}_{-0.00000}$	$0.31097^{+0.00004}_{-0.00000}$	$0.31035^{+0.00007}_{-0.00000}$
$\rho_{\text{rock,mean}}$ (kg m <sup>-3</sup> )	1364	3071	3058
$T_b$ (K)	265.0	269.4	269.4
$q_{\text{surf}}$ (mW m <sup>-2</sup> )	2.8	10.4	9.6
$q_{\text{con}}$ (mW m <sup>-2</sup> )	9.4	14.1	13.5
$\eta_{\text{con}}$ (Pa s)	$3.58 \times 10^{14}$	$2.66 \times 10^{14}$	$2.66 \times 10^{14}$
$D_{\text{Ih}}$ (km)	86.6	111.1	121.3
$D_{\text{ocean}}$ (km)	0.0	120.8	122.7
$\bar{\sigma}_{\text{ocean}}$ (S m <sup>-1</sup> )	-	0.9	0.9
$R_{\text{surf}}$ (km)	763.5	788.9	761.4
$R_{\text{rock}}$ (km)	676.9	557.0	517.4
$\phi_{\text{rock}}$	0.92	0.10	0.10

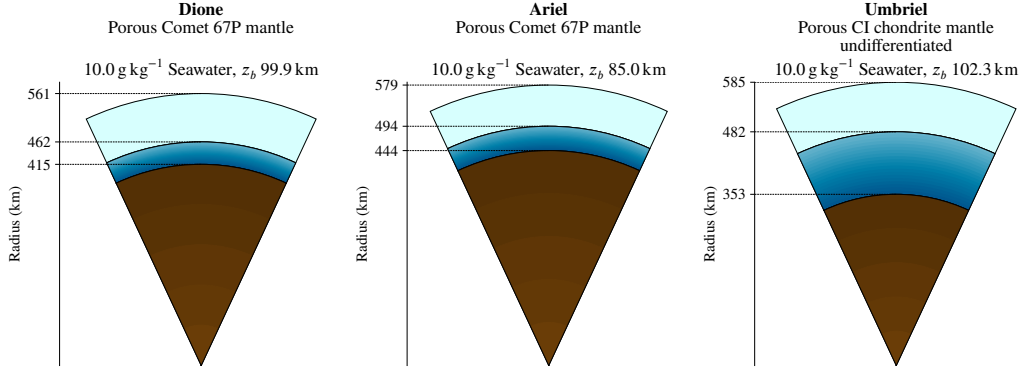


**Figure 8.** Wedge diagram showing major material layers for default models of small moons Dione, Ariel, and Umbriel, to scale. The depicted models are as summarized in Table 8; layer colors are indicated as described in Figure 5.

**Table 8.** *PlanetProfile* output summary for default models of small moons Dione, Ariel, and Umbriel. Material layers are depicted in Figure 8. Variable definitions are as in Table 5.

	Dione	Ariel	Umbriel
Ocean comp.	10.0 g kg <sup>-1</sup> Seawater	10.0 g kg <sup>-1</sup> Seawater	10.0 g kg <sup>-1</sup> Seawater
$M$ (kg)	$1.0954 \times 10^{21}$	$1.3530 \times 10^{21}$	$1.1720 \times 10^{21}$
$M_{\text{model}}$ (kg)	$1.0946 \times 10^{21}$	$1.3526 \times 10^{21}$	$1.1696 \times 10^{21}$
$C/MR^2$	$0.33 \pm 0.01$	$0.306 \pm 0.03$	$0.319 \pm 0.03$
$C_{\text{model}}/MR^2$	$0.33005^{+0.00088}_{-0.00067}$	$0.32603^{+0.00042}_{-0.00000}$	$0.31893^{+0.00052}_{-0.00008}$
$\rho_{\text{rock,mean}}$ (kg m <sup>-3</sup> )	2246	2526	2894
$T_b$ (K)	270.93	270.93	270.93
$q_{\text{surf}}$ (mW m <sup>-2</sup> )	9.6	5.2	4.4
$q_{\text{con}}$ (mW m <sup>-2</sup> )	14.2	7.1	6.4
$\eta_{\text{con}}$ (Pa s)	$2.56 \times 10^{14}$	$2.45 \times 10^{14}$	$2.45 \times 10^{14}$
$D_{\text{Ih}}$ (km)	99.9	85.0	102.3
$D_{\text{ocean}}$ (km)	46.3	50.2	129.0
$\bar{\sigma}_{\text{ocean}}$ (S m <sup>-1</sup> )	0.9	0.9	0.9
$R_{\text{surf}}$ (km)	561.4	578.9	584.7
$R_{\text{rock}}$ (km)	415.2	443.7	353.4
$\phi_{\text{rock}}$	0.50	0.35	0.10

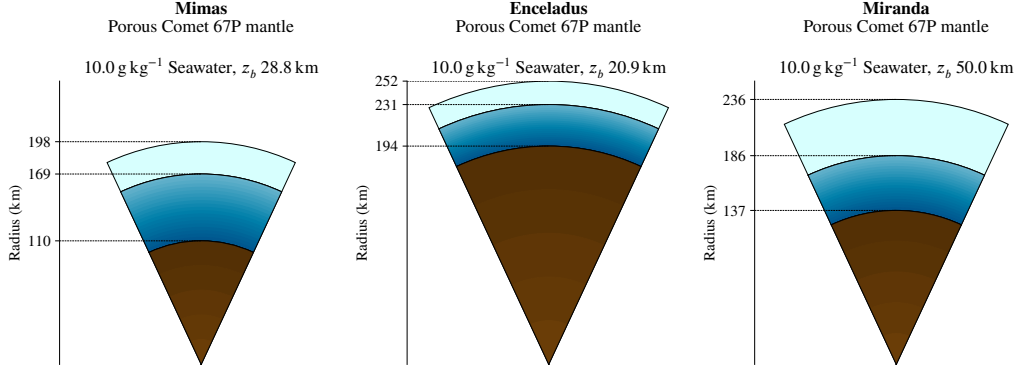


**Figure 9.** Wedge diagram showing major material layers for default models of the smallest large moons: Mimas, Enceladus, and Miranda, to scale. The depicted models are as summarized in Table 9; layer colors are indicated as described in Figure 5.

**Table 9.** *PlanetProfile* output summary for default models of the smallest large moons: Mimas, Enceladus, and Miranda. Material layers are depicted in Figure 9. Variable definitions are as in Table 5.

	Mimas	Enceladus	Miranda
Ocean comp.	10.0 g kg <sup>-1</sup> Seawater	10.0 g kg <sup>-1</sup> Seawater	10.0 g kg <sup>-1</sup> Seawater
$M$ (kg)	$3.7493 \times 10^{19}$	$1.0802 \times 10^{20}$	$6.5900 \times 10^{19}$
$M_{\text{model}}$ (kg)	$3.7423 \times 10^{19}$	$1.0777 \times 10^{20}$	$6.5866 \times 10^{19}$
$C/MR^2$	$0.355 \pm 0.01$	$0.335 \pm 0.001$	$0.35 \pm 0.03$
$C_{\text{model}}/MR^2$	$0.35487^{+0.00086}_{-0.00041}$	$0.33489^{+0.00000}_{-0.00020}$	$0.34500^{+0.00000}_{-0.00048}$
$\rho_{\text{rock,mean}}$ (kg m <sup>-3</sup> )	1994	2352	2181
$T_b$ (K)	272.5	272.4578	272.356
$q_{\text{surf}}$ (mW m <sup>-2</sup> )	17.6	23.1	9.4
$q_{\text{con}}$ (mW m <sup>-2</sup> )	24.1	27.4	15.1
$\eta_{\text{con}}$ (Pa s)	$2.40 \times 10^{14}$	$2.37 \times 10^{14}$	$2.28 \times 10^{14}$
$D_{\text{lh}}$ (km)	28.8	20.9	50.0
$D_{\text{ocean}}$ (km)	59.5	37.0	48.7
$\bar{\sigma}_{\text{ocean}}$ (S m <sup>-1</sup> )	1.0	1.0	1.0
$R_{\text{surf}}$ (km)	198.2	252.1	235.8
$R_{\text{rock}}$ (km)	110.0	194.3	137.0
$\phi_{\text{rock}}$	0.50	0.32	0.32

**Table 10.** Measured and assumed properties used in default models for the moons of Jupiter. The extreme pore closure pressure and rock porosity required to find a valid Callisto model imply that it is either far from hydrostatic equilibrium or contains extraordinarily low-density rock phases in its interior. The unrealistically low surface heat flux for Io is a requirement imposed by the current lack of a convection model for rocks in *PlanetProfile*. However, matching the MoI for this body suggests that the density structure is a reasonable match, so this model provides a starting point for future work, *e.g.*, with a manually adjusted thermal profile.

Property	Io	Europa	Ganymede	Callisto
Radius $R$ (km) <sup>a</sup>	1821.49	1560.8	2631.2	2410.3
Total mass $M$ (kg) <sup>b</sup>	$8.932 \times 10^{22}$	$4.800 \times 10^{22}$	$1.4819 \times 10^{23}$	$1.0759 \times 10^{23}$
Axial MoI $C/MR^2$	$0.37685 \pm 0.00035$ <sup>c</sup>	$0.346 \pm 0.005$ <sup>d</sup>	$0.3115 \pm 0.0028$ <sup>e</sup>	$0.3549^{+0.0042}_{-0.0148}$ <sup>f,g</sup>
Surface pressure $P_{\text{surf}}$ (MPa)	0	0	0	0
Surface temperature $T_{\text{surf}}$ (K)	110	110	110	110
Ocean composition and salinity $w$	N/A	$35.16504 \text{ g kg}^{-1}$ Seawater	Pure H <sub>2</sub> O	$100 \text{ g kg}^{-1}$ MgSO <sub>4</sub>
Ice bottom temperature $T_b$	N/A	268.305 K	258.86 K	262.0 K
Surface heat flux $q_{\text{surf}}$	$0.14 \text{ W m}^{-2}$	N/A	N/A	N/A
Rock composition	CV chondrite	CM chondrite	CM chondrite	Comet 67P/C-G
Core FeS/Fe ratio	12.5 wt% FeS	20 wt% FeS	20 wt% FeS	not modeled
Ice porosity in vacuum $\phi_{\text{ice}}$	N/A	not modeled	not modeled	not modeled
Ice pore closure pressure $P_{c,\text{ice}}$	-	-	-	-
Rock porosity in vacuum $\phi_{\text{rock}}$	70 vol%	not modeled	not modeled	90 vol%
Rock pore closure pressure $P_{c,\text{rock}}$	750 MPa	-	-	4000 MPa

<sup>a</sup> Mean radii from Archinal et al. (2018)

<sup>b</sup> Hussmann et al. (2006)

<sup>c</sup> Anderson, Jacobson, Lau, et al. (2001)

<sup>d</sup> Anderson et al. (1998)

<sup>e</sup> Schubert et al. (2004)

<sup>f</sup> Anderson, Jacobson, McElrath, et al. (2001)

<sup>g</sup> Lower value increased by 3% of mean value per Gao and Stevenson (2013)



**Table 11.** Measured and assumed properties used in default models for the moons of Saturn. As with Callisto, the large reported Mol values for Titan require extreme porosity conditions to achieve valid models that match reported mass and Mol values.

Property	Mimas	Enceladus	Dione	Rhea	Titan
Radius $R$ (km) <sup>a</sup>	198.2	252.1	561.4	763.5	2574.73
Total mass $M$ (kg) <sup>b</sup>	$3.7493 \times 10^{19}$	$1.08022 \times 10^{20}$	$1.095452 \times 10^{21}$	$2.306518 \times 10^{21}$	$1.3452 \times 10^{23}$
Axial Mol $C/MR^2$	$0.355 \pm 0.010$ <sup>c</sup>	$0.335 \pm 0.001$ <sup>d</sup>	$0.33 \pm 0.01$ <sup>e</sup>	$0.3721 \pm 0.0036$ <sup>f</sup>	$0.341^{+0.010}_{-0.020}$ <sup>g,h</sup>
Surface pressure $P_{\text{surf}}$ (MPa)	0	0	0	0	0.15
Surface temperature $T_{\text{surf}}$ (K)	80 <sup>i</sup>	75	75	75 <sup>j</sup>	94
Ocean composition and salinity $w$	$10 \text{ g kg}^{-1}$ Seawater	$10 \text{ g kg}^{-1}$ Seawater <sup>k</sup>	$10 \text{ g kg}^{-1}$ Seawater	$10 \text{ g kg}^{-1}$ Seawater	$100 \text{ g kg}^{-1}$ MgSO <sub>4</sub>
Ice bottom temperature $T_b$	$272.5 \text{ K}$ <sup>l</sup>	$272.4578 \text{ K}$	$270.93 \text{ K}$	$265.0 \text{ K}$ <sup>m</sup>	$255.0 \text{ K}$
Surface heat flux $q_{\text{surf}}$	N/A	N/A	N/A	N/A	N/A
Rock composition	Comet 67P/C-G	Comet 67P/C-G	Comet 67P/C-G	Comet 67P/C-G	Comet 67P/C-G
Core FeS/Fe ratio	not modeled	not modeled	not modeled	not modeled	not modeled
Ice porosity in vacuum $\phi_{\text{ice}}$	not modeled	not modeled	not modeled	not modeled	not modeled
Ice pore closure pressure $P_{c,\text{ice}}$	-	-	-	-	-
Rock porosity in vacuum $\phi_{\text{rock}}$	50 vol%	32 vol%	50 vol%	92 vol%	90 vol%
Rock pore closure pressure $P_{c,\text{rock}}$	350 MPa	350 MPa	350 MPa	550 MPa	2000 MPa

<sup>a</sup> Mean radii from Archinal et al. (2018)<sup>b</sup> Jacobson et al. (2006)<sup>c</sup> Hussmann et al. (2006); Tajeddine et al. (2014)<sup>d</sup> Iess et al. (2014)<sup>e</sup> Zannoni et al. (2020)<sup>f</sup> Iess et al. (2007)<sup>g</sup> Durante et al. (2019); uncertainty is not reported for this value<sup>h</sup> Lower value increased by 3% of mean value per Gao and Stevenson (2013)<sup>i</sup> Rhoden and Walker (2022)<sup>j</sup> Howett et al. (2010)<sup>k</sup> Glein et al. (2018)<sup>l</sup> Tajeddine et al. (2014)<sup>m</sup> Results in a completely frozen hydrosphere with  $T_b = 103 \text{ K}$

**Table 12.** Measured and assumed properties used in default models for the moons of Uranus.

Property	Miranda	Ariel	Umbriel	Titania	Oberon
Radius $R$ (km) <sup>a</sup>	235.8	578.9	584.7	788.9	761.4
Total mass $M$ (kg) <sup>b</sup>	$0.659 \times 10^{20}$	$1.353 \times 10^{21}$	$1.172 \times 10^{21}$	$3.527 \times 10^{21}$	$3.014 \times 10^{21}$
Axial MoI $C/MR^2$ <sup>c</sup>	$0.35 \pm 0.03$	$0.306 \pm 0.030$	$0.319 \pm 0.030$	$0.306 \pm 0.030$	$0.307 \pm 0.030$
Surface pressure $P_{\text{surf}}$ (MPa)	0	0	0	0	0
Surface temperature $T_{\text{surf}}$ (K)	60	60	60	60	60
Ocean composition and salinity $w$	$10 \text{ g kg}^{-1}$ Seawater	$10 \text{ g kg}^{-1}$ Seawater	$10 \text{ g kg}^{-1}$ Seawater	$10 \text{ g kg}^{-1}$ Seawater	$10 \text{ g kg}^{-1}$ Seawater
Ice bottom temperature $T_b$	272.356 K	270.93 K	270.93 K	269.4 K	269.4 K
Surface heat flux $q_{\text{surf}}$	N/A	N/A	N/A	N/A	N/A
Rock composition	Comet 67P/C-G	Comet 67P/C-G	CI chondrite	CI chondrite	CI chondrite
Core FeS/Fe ratio	not modeled	not modeled	not modeled	not modeled	not modeled
Ice porosity in vacuum $\phi_{\text{ice}}$	not modeled	not modeled	not modeled	not modeled	not modeled
Ice pore closure pressure $P_{\text{c,ice}}$	-	-	-	-	-
Rock porosity in vacuum $\phi_{\text{rock}}$	32 vol%	35 vol%	10 vol%	10 vol%	10 vol%
Rock pore closure pressure $P_{\text{c,rock}}$	350 MPa	450 MPa	450 MPa	450 MPa	450 MPa

<sup>a</sup> Mean radii from Archinal et al. (2018)<sup>b</sup> Jacobson et al. (1992)<sup>c</sup> Hussmann et al. (2006); large uncertainties estimated based on source methods

**Table 13.** Measured and assumed properties used in default models for Triton and Pluto.

Property	Triton	Pluto
Radius $R$ (km) <sup>a</sup>	1352.6	1188.3
Total mass $M$ (kg)	$2.141 \times 10^{22}$ <sup>b</sup>	$1.303 \times 10^{22}$ <sup>c</sup>
Axial MoI $C/MR^2$	$0.31 \pm 0.03$ <sup>d</sup>	$0.31 \pm 0.03$
Surface pressure $P_{\text{surf}}$ (MPa)	0	0
Surface temperature $T_{\text{surf}}$ (K)	38	44
Ocean composition and salinity $w$	$10 \text{ g kg}^{-1} \text{ MgSO}_4$	$50 \text{ g kg}^{-1} \text{ MgSO}_4$
Ice bottom temperature $T_b$	266.0 K	265.0 K
Surface heat flux $q_{\text{surf}}$	N/A	N/A
Rock composition	Comet 67P/C–G	Comet 67P/C–G
Core FeS/Fe ratio	not modeled	not modeled
Ice porosity in vacuum $\phi_{\text{ice}}$	not modeled	not modeled
Ice pore closure pressure $P_{c,\text{ice}}$	-	-
Rock porosity in vacuum $\phi_{\text{rock}}$	35 vol%	35 vol%
Rock pore closure pressure $P_{c,\text{rock}}$	350 MPa	350 MPa

<sup>a</sup> Mean radii from Archinal et al. (2018)<sup>b</sup> Tyler et al. (1989)<sup>c</sup> Brozović et al. (2015)<sup>d</sup> Hussmann et al. (2006); large uncertainties estimated based on source methods

Future investigations of icy bodies will rely heavily on gravitational fields, magnetic fields, and remote sensing to constrain their interior structures. *PlanetProfile* is the only open-source software yet available that self-consistently relates bulk properties of icy bodies derived from spacecraft gravity measurements—through an ocean EOS including electrical conductivity—to the induced magnetic fields expected from their subsurface oceans. Integration with other open-source software packages is essential to this key feature. Incorporating measurements from as many sources as possible to better constrain the results is vital, and represents a major motivation for the design of *PlanetProfile*.

Because *PlanetProfile* models rely on laboratory measurements to inform the ocean and pore fluid EOS, the models are limited to those compositions for which such measurements exist or can be reliably extrapolated into the regions of interest. Due to the lack of suitable measurements in many pure (binary) and all mixed aqueous systems, the modeled oceans are restricted to a handful of end-member cases for their solutes, and for larger bodies, only a single dissolved solute type can be studied.

Clathrates of volatile species (*e.g.*, CH<sub>4</sub> and CO<sub>2</sub>) and ions are likely common in the outer solar system (Hand et al., 2006; Journaux et al., 2013; Mousis et al., 2015). Measurements of clathrates at relevant conditions are also lacking, especially for mixtures of guest molecules and amalgamated layers of ice and clathrates. Laboratory measurements of the relevant properties of these materials can dramatically affect models that incorporate them, especially when the alternative is to omit materials with insufficient data.

*PlanetProfile* currently does not model convection in rock layers. Not including this process restricts the applicability of fully self-consistent models to those that do not reach internal temperatures warm enough to convect. Such assumptions have typically been regarded as valid because of the prevailing view that tidally generated heat concentrates in the icy lithosphere (Tobie et al., 2005; Kang & Flierl, 2020). This view has been challenged by inferences of hydrothermal minerals in the Enceladus E-ring (Hsu et al., 2015) and recent 3D models of Europa’s tides (Běhouňková et al., 2021), opening a larger parameter space of models to explore in future work. In these cases, the current release of *PlanetProfile* remains useful for exploring planetary properties, especially for bodies with substantial overlying oceans.

Convection is important for bodies like Io with a high surface heat flux, although here as well convection may be limited in favor of heat transport through melt migration (Moore, 2003). The mass- and MoI-matching density profile evaluated with *PlanetProfile* for non-convecting bodies offers a valuable starting point for further modeling to improve self-consistency. Implementing self-consistent convection in rocks is a top priority for future development. In addition, modeling of partial melts will allow investigation of unresolved questions at Io, including whether a magma ocean may be present there (Khurana et al., 2011) despite the challenges this presents to meet the relatively high mantle viscosity (of order  $10^{16}$  Pa s) needed to sustain the observed surface heat flux of  $2.24 \text{ W m}^{-2}$  (Lainey et al., 2009).

For partially differentiated bodies like Callisto, Rhea, and Titan, mixed ice/fluid/rock interior layers are modeled using an effective porosity. Deep inside Callisto and Titan, the great overburden pressure should tend to close pores, consistent with models for thermally induced and tectonic fracturing (Vance et al., 2007; Klimczak et al., 2019). The porosity model we employ (Han et al., 2014) requires very large pore closure pressures and vacuum-equivalent porosities in order to generate valid profiles that match the high MoIs. This result has a few possible implications: 1) The rock matrix includes very low-density silicates or large amounts of high-pressure ices or both. A mixed ice-rock “snowball” has been suggested as an explanation for Callisto (Schubert et al., 2004), which fits with this interpretation. 2) The bodies are very homogeneous in their interiors. Such homogeneity requires low-density mineralogies. The carbonaceous silicate interior model for Titan suggested by Néri et al. (2020) offers one such scenario. 3) The Han et al. (2014) exponential model is not valid for the mixed material phases that we assume. Alternative porosity models must still account for the migration and fate of volatiles and ices in the rocky interiors of large ocean worlds. Related studies of Europa’s early metamorphic outgassing in relation to the formation of its ocean retain extensive volatiles in the rocky interior without quantifying the implied porosities involved (Melwani Daswani et al., 2021).

Converting the ocean melting temperature input to a surface heat flux input for ice shells, and self-consistently calculating convection from these, is another top priority for future development. Valid models for Rhea suggest it has a completely frozen hydrosphere, but the temperature at the ice-rock interface cannot be determined self-consistently in *PlanetProfile* because the ocean melting temperature is a model input. This present

limitation adds uncertainty to the rock densities determined from the EOS for Rhea, and hence the mass- and MoI-matching are biased to structural solutions that include oceans.

*PlanetProfile* is a versatile tool that can be applied to study a wide array of problems in understanding planetary bodies in the solar system and beyond. The software is open-source and frequently updated. As more laboratory measurements become available, it will be possible to use *PlanetProfile* to explore an ever-greater space of possible configurations.

## Open Research

Data used in this work were generated using the open-source *PlanetProfile* software hosted on GitHub. A Zenodo archive of the most recent version is available at <https://doi.org/10.5281/zenodo.844130> (Styczinski, Vance, Niesyt, et al., 2022). *PlanetProfile* is released under a GNU GPL-v3.0 license. The v2.3.3 release associated with this manuscript is archived at <https://doi.org/10.5281/zenodo.7319838> (Styczinski, Vance, Niesyt, et al., 2022). A Zenodo archive of the output data for default models is available at <https://doi.org/10.5281/zenodo.7250785> (Styczinski, Vance, & Daswani, 2022a). A Zenodo archive of models generated for comparison to Vance et al. (2018) is available at <https://doi.org/10.5281/zenodo.7318029> (Styczinski, Vance, & Daswani, 2022b). The v1.0.0 release associated with Vance et al. (2018) is archived at <https://doi.org/10.5281/zenodo.844131> (Vance, 2017).

## Acknowledgments

M.J.S. thanks S. Stähler for direction on creating files compatible with *AxiSEM*, A. Bryant and M. Panning for the same with *Mineos*, and E. Leonard and S. Eilenberg for helpful discussions. This work was carried out at the Jet Propulsion Laboratory, California Institute of Technology, under a contract with NASA (80NM0018D0004). The authors acknowledge that portions of this work have been carried out on the traditional lands of the Tongva people. M.J.S. was supported by an appointment to the NASA Postdoctoral Program at the Jet Propulsion Laboratory, California Institute of Technology, administered by Oak Ridge Associated Universities under a contract with NASA (80HQTR21CA005). M.M.D. was supported by NASA grant NNH18ZDA001N-HW:Habitable Worlds and NASA Planetary Science Early Career Award NNH19ZDA001N-ECA.

## References

- Anderson, J. D., Jacobson, R. A., Lau, E. L., Moore, W. B., & Schubert, G. (2001). Io's gravity field and interior structure. *Journal of Geophysical Research: Planets*, *106*(E12), 32963–32969.
- Anderson, J. D., Jacobson, R. A., McElrath, T. P., Moore, W. B., Schubert, G., & Thomas, P. C. (2001). Shape, mean radius, gravity field, and interior structure of Callisto. *Icarus*, *153*(1), 157–161.
- Anderson, J. D., Lau, E. L., Sjogren, W. L., Schubert, G., & Moore, W. B. (1996). Gravitational constraints on the internal structure of Ganymede. *Nature*, *384*(6609), 541–543.
- Anderson, J. D., Schubert, G., Jacobson, R. A., Lau, E. L., Moore, W. B., & Sjogren, W. L. (1998). Europa's differentiated internal structure: Inferences from four Galileo encounters. *Science*, *281*(5385), 2019–2022. doi: 10.1126/science.281.5385.2019
- Andersson, O., & Inaba, A. (2005). Thermal conductivity of crystalline and amorphous ices and its implications on amorphization and glassy water. *Physical Chemistry Chemical Physics*, *7*(7), 1441–1449.
- Archinal, B. A., Acton, C. H., A'Hearn, M. F., Conrad, A., Consolmagno, G. J., Duxbury, T., ... Williams, I. P. (2018). Report of the IAU working group on cartographic coordinates and rotational elements: 2015. *Celestial Mechanics and Dynamical Astronomy*, *130*(3), 22. doi: 10.1007/s10569-017-9805-5
- Bardyn, A., Baklouti, D., Cottin, H., Fray, N., Briois, C., Paquette, J., ... Hilchenbach, M. (2017). Carbon-rich dust in comet 67P/Churyumov-Gerasimenko measured by COSIMA/Rosetta. *Monthly Notices of the Royal Astronomical Society*, *469*(Suppl.2), S712–S722.
- Běhouňková, M., Tobie, G., Choblet, G., Kervazo, M., Daswani, M. M., Dumoulin, C., & Vance, S. D. (2021). Tidally induced magmatic pulses on the oceanic floor of Jupiter's moon Europa. *Geophysical Research Letters*, *48*(3). Retrieved from <https://doi.org/10.1029/2020gl090077> doi: 10.1029/2020gl090077
- Beuthe, M., Rivoldini, A., & Trinh, A. (2016). Enceladus's and Dione's floating ice shells supported by minimum stress isostasy. *Geophysical Research Letters*, *43*(19), 10–088.

- 837 Beyreuther, M., Barsch, R., Krischer, L., Megies, T., Behr, Y., & Wassermann, J.  
838 (2010). ObsPy: A Python toolbox for seismology. *Seismological Research*  
839 *Letters*, 81(3), 530–533.
- 840 Bollengier, O., Brown, J. M., & Shaw, G. H. (2019). Thermodynamics of pure liquid  
841 water: Sound speed measurements to 700 MPa down to the freezing point, and  
842 an equation of state to 2300 MPa from 240 to 500 K. *The Journal of Chemical*  
843 *Physics*, 151(5), 054501.
- 844 Brozović, M., Showalter, M. R., Jacobson, R. A., & Buie, M. W. (2015). The orbits  
845 and masses of satellites of Pluto. *Icarus*, 246, 317–329.
- 846 Chatterjee, N. D., & Froese, E. (1975). A thermodynamic study of the pseudobinary  
847 join muscovite-paragonite in the system  $\text{KAlSi}_3\text{O}_8$ - $\text{NaAlSi}_3\text{O}_8$ - $\text{Al}_2\text{O}_3$ - $\text{SiO}_2$ -  
848  $\text{H}_2\text{O}$ . *American Mineralogist*, 60(11-12), 985–993.
- 849 Choukroun, M., & Grasset, O. (2010). Thermodynamic data and modeling of  
850 the water and ammonia–water phase diagrams up to 2.2 GPa for planetary  
851 geophysics. *The Journal of chemical physics*, 133(14), 144502.
- 852 Choukroun, M., Grasset, O., Tobie, G., & Sotin, C. (2010). Stability of methane  
853 clathrate hydrates under pressure: Influence on outgassing processes of  
854 methane on Titan. *Icarus*, 205(2), 581–593.
- 855 Cockell, C. S., Bush, T., Bryce, C., Direito, S., Fox-Powell, M., Harrison, J. P., ...  
856 Zorzano, M. P. (2016). Habitability: A Review. *Astrobiology*, 16(1), 89–117.  
857 doi: 10.1089/ast.2015.1295
- 858 Connolly, J. A. D. (2009). The geodynamic equation of state: what and how. *Geo-*  
859 *chemistry, geophysics, geosystems*, 10(10).
- 860 Connolly, J. A. D., & Galvez, M. E. (2018). Electrolytic fluid speciation by Gibbs  
861 energy minimization and implications for subduction zone mass transfer. *Earth*  
862 *and Planetary Science Letters*, 501, 90–102. doi: 10.1016/j.epsl.2018.08.024
- 863 Cottaar, S., Heister, T., Rose, I., & Unterborn, C. (2014). BurnMan: A lower mantle  
864 mineral physics toolkit. *Geochemistry, Geophysics, Geosystems*, 15(4), 1164–  
865 1179.
- 866 Crotwell, H. P., Owens, T. J., & Ritsema, J. (1999). The TauP Toolkit: Flexible  
867 seismic travel-time and ray-path utilities. *Seismological Research Letters*, 70,  
868 154–160. doi: 10.1785/gssrl.70.2.154
- 869 Deschamps, F., & Sotin, C. (2001). Thermal convection in the outer shell of large



- 870 icy satellites. *Journal of Geophysical Research: Planets*, 106(E3), 5107–5121.
- 871 Dhooghe, F., De Keyser, J., Altwegg, K., Briois, C., Balsiger, H., Berthelier, J.-J.,  
 872 ... Wurz, P. (2017). Halogens as tracers of protosolar nebula material in  
 873 comet 67P/Churyumov–Gerasimenko. *Monthly Notices of the Royal Astronom-*  
 874 *ical Society*, 472(2), 1336–1345.
- 875 Durante, D., Hemingway, D. J., Racioppa, P., Iess, L., & Stevenson, D. J. (2019).  
 876 Titan’s gravity field and interior structure after Cassini. *Icarus*, 326, 123–132.
- 877 Dziewonski, A. M., & Anderson, D. L. (1981). Preliminary reference Earth model.  
 878 *Physics of the earth and planetary interiors*, 25(4), 297–356.
- 879 Feistel, R., & Wagner, W. (2006). A new equation of state for H<sub>2</sub>O ice Ih. *Journal of*  
 880 *Physical and Chemical Reference Data*, 35(2), 1021–1047.
- 881 Filacchione, G., Groussin, O., Herny, C., Kappel, D., Mottola, S., Oklay, N., ...  
 882 Raponi, A. (2019). Comet 67P/CG nucleus composition and comparison to  
 883 other comets. *Space science reviews*, 215(1), 1–46.
- 884 Gao, P., & Stevenson, D. J. (2013). Nonhydrostatic effects and the determination of  
 885 icy satellites’ moment of inertia. *Icarus*, 226(2), 1185–1191.
- 886 Glein, C. R., Postberg, F., & Vance, S. D. (2018). The geochemistry of Enceladus:  
 887 composition and controls. In P. M. Schenk, R. N. Clark, C. J. A. Howett,  
 888 A. J. Verbiscer, & J. H. Waite (Eds.), *Enceladus and the icy moons of Saturn*  
 889 (pp. 39–56). Tucson: University of Arizona Press.
- 890 Glein, C. R., & Waite, J. H. (2020). The carbonate geochemistry of Enceladus’  
 891 ocean. *Geophysical Research Letters*, 47(3), e2019GL085885.
- 892 Glover, P. W. J., & Vine, F. J. (1994). Electrical conductivity of the continental  
 893 crust. *Geophysical research letters*, 21(22), 2357–2360.
- 894 Green, E., Holland, T. J. B., & Powell, R. (2007). An order-disorder model for  
 895 omphacitic pyroxenes in the system jadeite-diopside-hedenbergite-acmite, with  
 896 applications to eclogitic rocks. *American Mineralogist*, 92(7), 1181–1189. doi:  
 897 10.2138/am.2007.2401
- 898 Hammond, N. P., Barr, A. C., & Parmentier, E. M. (2016). Recent tectonic ac-  
 899 tivity on Pluto driven by phase changes in the ice shell. *Geophysical Research*  
 900 *Letters*, 43(13), 6775–6782.
- 901 Han, S.-C., Schmerr, N., Neumann, G., & Holmes, S. (2014). Global characteristics  
 902 of porosity and density stratification within the lunar crust from GRAIL grav-

- ity and Lunar Orbiter Laser Altimeter topography data. *Geophysical Research Letters*, 41(6), 1882–1889.
- Hand, K., Chyba, C., Carlson, R., & Cooper, J. (2006). Clathrate Hydrates of Oxidants in the Ice Shell of Europa. *Astrobiology*, 6(3), 463–482.
- Helgerud, M., Waite, W. F., Kirby, S., & Nur, A. (2009). Elastic wave speeds and moduli in polycrystalline ice Ih, sI methane hydrate, and sII methane-ethane hydrate. *Journal of Geophysical Research: Solid Earth*, 114(B2).
- Hemingway, D. J., & Mittal, T. (2019). Enceladus’s ice shell structure as a window on internal heat production. *Icarus*, 332, 111–131.
- Holland, T. J. B., Baker, J., & Powell, R. (1998). Mixing properties and activity-composition relationships of chlorites in the system MgO-FeO-Al<sub>2</sub>O<sub>3</sub>-SiO<sub>2</sub>-H<sub>2</sub>O. *European Journal of Mineralogy*, 10(3), 395–406. doi: 10.1127/ejm/10/3/0395
- Holland, T. J. B., Green, E. C. R., & Powell, R. (2018). Melting of peridotites through to granites: A simple thermodynamic model in the system KNCF-MASHTOCr. *Journal of Petrology*, 59(5), 881–900. doi: 10.1093/petrology/egy048
- Holland, T. J. B., & Powell, R. (1998). An internally consistent thermodynamic data set for phases of petrological interest. *Journal of metamorphic Geology*, 16(3), 309–343.
- Holland, T. J. B., & Powell, R. (2011). An improved and extended internally consistent thermodynamic dataset for phases of petrological interest, involving a new equation of state for solids. *Journal of Metamorphic Geology*, 29, 333.
- Howett, C. J. A., Spencer, J. R., Pearl, J., & Segura, M. (2010). Thermal inertia and bolometric Bond albedo values for Mimas, Enceladus, Tethys, Dione, Rhea and Iapetus as derived from Cassini/CIRS measurements. *Icarus*, 206(2), 573–593.
- Hsu, H.-W., Postberg, F., Sekine, Y., Shibuya, T., Kempf, S., Horányi, M., . . . Srama, R. (2015). Ongoing hydrothermal activities within Enceladus. *Nature*, 519(7542), 207–210.
- Husmann, H., Sohl, F., & Spohn, T. (2006). Subsurface oceans and deep interiors of medium-sized outer planet satellites and large trans-neptunian objects. *Icarus*, 185(1), 258–273.

- 936 Iess, L., Rappaport, N. J., Tortora, P., Lunine, J., Armstrong, J. W., Asmar, S. W.,  
 937 ... Zingoni, F. (2007). Gravity field and interior of Rhea from Cassini data  
 938 analysis. *Icarus*, 190(2), 585–593.
- 939 Iess, L., Stevenson, D., Parisi, M., Hemingway, D., Jacobson, R., Lunine, J., ... Tor-  
 940 tora, P. (2014). The gravity field and interior structure of Enceladus. *Science*,  
 941 344(6179), 78–80.
- 942 Jacobson, R. A., Antreasian, P. G., Bordi, J. J., Criddle, K. E., Ionasescu, R., Jones,  
 943 J. B., ... Stauch, J. R. (2006). The gravity field of the saturnian system from  
 944 satellite observations and spacecraft tracking data. *The Astronomical Journal*,  
 945 132(6), 2520.
- 946 Jacobson, R. A., Campbell, J. K., Taylor, A. H., & Synnott, S. P. (1992). The  
 947 masses of Uranus and its major satellites from Voyager tracking data and  
 948 Earth-based Uranian satellite data. *The Astronomical Journal*, 103, 2068–  
 949 2078.
- 950 Jennings, E. S., Holland, T. J. B., Shorttle, O., MacLennan, J., & Gibson, S. A.  
 951 (2016). The composition of melts from a heterogeneous mantle and the origin  
 952 of ferropicrite: Application of a thermodynamic model. *Journal of Petrology*,  
 953 57, 2289–2310. doi: 10.1093/petrology/egw065
- 954 Journaux, B., Brown, J. M., Pakhomova, A., Collings, I. E., Petitgirard, S., Es-  
 955 pinoza, P., ... Hanfland, M. (2020). Holistic approach for studying planetary  
 956 hydrospheres: Gibbs representation of ices thermodynamics, elasticity, and the  
 957 water phase diagram to 2,300 MPa. *Journal of Geophysical Research: Planets*,  
 958 125(1), e2019JE006176.
- 959 Journaux, B., Daniel, I., Caracas, R., Montagnac, G., & Cardon, H. (2013). Influ-  
 960 ence of NaCl on ice VI and ice VII melting curves up to 6 GPa, implications  
 961 for large icy moons. *Icarus*, 226(1), 355–363.
- 962 Kamata, S., Nimmo, F., Sekine, Y., Kuramoto, K., Noguchi, N., Kimura, J., & Tani,  
 963 A. (2019). Pluto’s ocean is capped and insulated by gas hydrates. *Nature*  
 964 *Geoscience*, 12(6), 407–410.
- 965 Kang, W., & Flierl, G. (2020). Spontaneous formation of geysers at only one pole  
 966 on Enceladus’s ice shell. *Proceedings of the National Academy of Sciences*,  
 967 117(26), 14764–14768.
- 968 Khurana, K. K., Jia, X., Kivelson, M. G., Nimmo, F., Schubert, G., & Russell, C. T.

- (2011). Evidence of a global magma ocean in Io's interior. *Science*, *332*(6034), 1186–1189.
- Khurana, K. K., Kivelson, M. G., & Russell, C. T. (2002). Searching for liquid water in Europa by using surface observatories. *Astrobiology*, *2*(1), 93–103. doi: 10.1089/153110702753621376
- Kimura, J., & Kamata, S. (2020). Stability of the subsurface ocean of Pluto. *Planetary and Space Science*, *181*, 104828.
- Kivelson, M. G., Khurana, K. K., Russell, C. T., Volwerk, M., Walker, R. J., & Zimmer, C. (2000). Galileo magnetometer measurements: A stronger case for a subsurface ocean at Europa. *Science*, *289*(5483), 1340–1343. doi: 10.1126/science.289.5483.1340
- Klimczak, C., Byrne, P. K., Regensburger, P. V., Bohnenstiehl, D. R., Hauck, S. A., Dombard, A. J., ... Elder, C. M. (2019). Strong ocean floors within Europa, Titan, and Ganymede limit geological activity there; Enceladus less so. In *50th annual lunar and planetary science conference* (p. 2912).
- Lainey, V., Arlot, J.-E., Karatekin, Ö., & Van Hoolst, T. (2009). Strong tidal dissipation in Io and Jupiter from astrometric observations. *Nature*, *459*(7249), 957–959.
- Larionov, E., & Kryukov, P. (1984). The conductivity of  $\text{MgSO}_4$  aqueous-solutions in the range of temperatures 298–423 K and pressures 0.1–784.6 MPa. *Izvestiya Sibirskogo Otdeleniya Akademii Nauk SSSR Seriya Khimicheskikh Nauk*, *5*, 20–23.
- Le Roy, L., Altwegg, K., Balsiger, H., Berthelier, J.-J., Bieler, A., Briois, C., ... Tzou, C.-y. (2015). Inventory of the volatiles on comet 67P/Churyumov-Gerasimenko from Rosetta/ROSINA. *Astronomy & Astrophysics*, *583*, A1.
- Light, T. S., Licht, S., Bevilacqua, A. C., & Morash, K. R. (2004). The fundamental conductivity and resistivity of water. *Electrochemical and solid-state letters*, *8*(1), E16.
- Lodders, K. (2021). Relative atomic solar system abundances, mass fractions, and atomic masses of the elements and their isotopes, composition of the solar photosphere, and compositions of the major chondritic meteorite groups. *Space Science Reviews*, *217*(3), 44. doi: 10.1007/s11214-021-00825-8
- Lodders, K., & Fegley, B. (1998). *The planetary scientist's companion*. Oxford Uni-

- 1002           versity Press on Demand.
- 1003   McDougall, T. J., & Barker, P. M.   (2011).   Getting started with TEOS-10 and the
- 1004           Gibbs seawater (GSW) oceanographic toolbox.   *SCOR/IAPSO WG, 127*, 1–
- 1005           28.
- 1006   McKinnon, W. B.   (2006).   On convection in ice I shells of outer solar system bodies,
- 1007           with detailed application to Callisto. *Icarus, 183*(2), 435–450.
- 1008   Melini, D., Saliby, C., & Spada, G.   (2022).   On computing viscoelastic Love numbers
- 1009           for general planetary models: the ALMA3 code.   *Geophysical Journal Interna-*
- 1010           *tional, 231*(3), 1502–1517.
- 1011   Melosh, H. J., Ekholm, A. G., Showman, A. P., & Lorenz, R. D.   (2004).   The tem-
- 1012           perature of Europa’s subsurface water ocean. *Icarus, 168*(2), 498–502.
- 1013   Melwani Daswani, M., Vance, S. D., Mayne, M. J., & Glein, C. R.   (2021).   A meta-
- 1014           morphic origin for Europa’s ocean. *Geophysical Research Letters*. (under revi-
- 1015           sion)
- 1016   Moore, W. B.   (2003).   Tidal heating and convection in Io. *Journal of Geophysical*
- 1017           *Research: Planets, 108*(E8), 5096.
- 1018   Morin, D.   (2008).   *Introduction to classical mechanics: with problems and solutions*.
- 1019           Cambridge University Press.
- 1020   Mousis, O., Chassefière, E., Holm, N. G., Bouquet, A., Waite, J. H., Geppert,
- 1021           W. D., . . . Rousselot, P.   (2015).   Methane clathrates in the solar system.
- 1022           *Astrobiology, 15*(4), 308–326. doi: 10.1089/ast.2014.1189
- 1023   Néri, A., Guyot, F., Reynard, B., & Sotin, C.   (2020).   A carbonaceous chondrite and
- 1024           cometary origin for icy moons of Jupiter and Saturn. *Earth and Planetary Sci-*
- 1025           *ence Letters, 530*, 115920.
- 1026   Nimmo, F., Hamilton, D. P., McKinnon, W. B., Schenk, P. M., Binzel, R. P., Bier-
- 1027           son, C. J., . . . The New Horizons Geology, Geophysics & Imaging Theme
- 1028           Team   (2016).   Reorientation of Sputnik Planitia implies a subsurface ocean on
- 1029           Pluto. *Nature, 540*(7631), 94–96.
- 1030   Nimmo, F., & Pappalardo, R. T.   (2016).   Ocean worlds in the outer solar system.
- 1031           *Journal of Geophysical Research: Planets, 121*(8), 1378–1399.
- 1032   Ning, F., Glavatskiy, K., Ji, Z., Kjelstrup, S., & Vlugt, T. H.   (2015).   Compress-
- 1033           ibility, thermal expansion coefficient and heat capacity of  $\text{CH}_4$  and  $\text{CO}_2$  hydrate
- 1034           mixtures using molecular dynamics simulations. *Physical Chemistry Chemical*

- 1035 *Physics*, 17(4), 2869–2883.
- 1036 Nissen-Meyer, T., van Driel, M., Stähler, S. C., Hosseini, K., Hempel, S., Auer,  
1037 L., ... Fournier, A. (2014). AxiSEM: broadband 3-D seismic wavefields in  
1038 axisymmetric media. *Solid Earth*, 5(1), 425–445.
- 1039 Padrón-Navarta, J. A., Sánchez-Vizcaíno, V. L., Hermann, J., Connolly, J. A., Gar-  
1040 rido, C. J., Gómez-Pugnaire, M. T., & Marchesi, C. (2013). Tschermak’s  
1041 substitution in antigorite and consequences for phase relations and water lib-  
1042 eration in high-grade serpentinites. *Serpentinites from mid-oceanic ridges to*  
1043 *subduction*, 178, 186–196. doi: 10.1016/j.lithos.2013.02.001
- 1044 Pätzold, M., Andert, T., Hahn, M., Asmar, S. W., Barriot, J.-P., Bird, M. K., ...  
1045 Scholten, F. (2016). A homogeneous nucleus for comet 67P/Churyumov–  
1046 Gerasimenko from its gravity field. *Nature*, 530(7588), 63–65.
- 1047 Petrenko, V. F., & Schulson, E. M. (1992). The effect of static electric fields on pro-  
1048 tonic conductivity of ice single crystals. *Philosophical Magazine B*, 66(3), 341–  
1049 353.
- 1050 Pozzo, M., Davies, C., Gubbins, D., & Alfè, D. (2012). Thermal and electrical con-  
1051 ductivity of iron at Earth’s core conditions. *Nature*, 485(7398), 355–358.
- 1052 Quist, A. S., & Marshall, W. L. (1968). Electrical conductances of aqueous sodium  
1053 chloride solutions from 0 to 800° and at pressures to 4000 bars. *The journal of*  
1054 *physical chemistry*, 72(2), 684–703.
- 1055 Rambaux, N., & Castillo-Rogez, J. (2013). Tides on satellites of giant plan-  
1056 ets. In J. Souchay, S. Mathis, & T. Tokieda (Eds.), *Tides in astronomy*  
1057 *and astrophysics* (pp. 167–200). Springer-Verlag Berlin Heidelberg. doi:  
1058 10.1007/978-3-642-32961-6\_5
- 1059 Rhoden, A. R., & Walker, M. E. (2022). The case for an ocean-bearing Mimas from  
1060 tidal heating analysis. *Icarus*, 376, 114872.
- 1061 Rothschild, L. J., & Mancinelli, R. L. (2001). Life in extreme environments. *Nature*,  
1062 409(6823), 1092–1101.
- 1063 Saxena, S., & Eriksson, G. (2015). Thermodynamics of Fe–S at ultra-high pressure.  
1064 *Calphad*, 51, 202–205. doi: 10.1016/j.calphad.2015.09.009
- 1065 Schubert, G., Anderson, J. D., Spohn, T., & McKinnon, W. B. (2004). Interior  
1066 composition, structure and dynamics of the Galilean satellites. In F. Bage-  
1067 nal, T. Dowling, & W. McKinnon (Eds.), *Jupiter: The planet, satellites and*

- 1068 *magnetosphere* (pp. 281–306). Cambridge University Press.
- 1069 Sloan, E. (1998). Physical/chemical properties of gas hydrates and application to  
 1070 world margin stability and climatic change. *Geological society, London, special*  
 1071 *publications*, 137(1), 31–50.
- 1072 Solomatov, V. S. (1995). Scaling of temperature-and stress-dependent viscosity con-  
 1073 vection. *Physics of Fluids*, 7(2), 266–274.
- 1074 Spada, G. (2008). ALMA, a Fortran program for computing the viscoelastic Love  
 1075 numbers of a spherically symmetric planet. *Computers & Geosciences*, 34(6),  
 1076 667–687.
- 1077 Stähler, S. C., Panning, M. P., Vance, S. D., Lorenz, R. D., van Driel, M., Nissen-  
 1078 Meyer, T., & Kedar, S. (2018). Seismic wave propagation in icy ocean worlds.  
 1079 *Journal of Geophysical Research: Planets*, 123(1), 206–232.
- 1080 Staley, D. O. (1970). The adiabatic lapse rate in the Venus atmosphere. *Journal of*  
 1081 *the Atmospheric Sciences*, 27(2), 219–223.
- 1082 Stern, L. A., Constable, S., Lu, R., Du Frane, W. L., & Roberts, J. J. (2021).  
 1083 Electrical properties of carbon dioxide hydrate: Implications for monitoring  
 1084 CO<sub>2</sub> in the gas hydrate stability zone. *Geophysical Research Letters*, 48(15),  
 1085 e2021GL093475.
- 1086 Styczinski, M. J., Vance, S. D., & Daswani, M. M. (2022a). *Planetprofile default*  
 1087 *model outputs* [Dataset]. Zenodo. Retrieved from [https://doi.org/10.5281/](https://doi.org/10.5281/zenodo.7319854)  
 1088 [zenodo.7319854](https://doi.org/10.5281/zenodo.7319854) doi: 10.5281/zenodo.7319854
- 1089 Styczinski, M. J., Vance, S. D., & Daswani, M. M. (2022b). *PlanetProfile Python*  
 1090 *version outputs compared to models of Vance et al. (2018)* [Dataset]. Zenodo.  
 1091 Retrieved from <https://doi.org/10.5281/zenodo.7318030> doi: 10.5281/  
 1092 [zenodo.7318030](https://doi.org/10.5281/zenodo.7318030)
- 1093 Styczinski, M. J., Vance, S. D., Harnett, E. M., & Cochrane, C. J. (2022). A per-  
 1094 turbation method for evaluating the magnetic field induced from an arbitrary,  
 1095 asymmetric ocean world analytically. *Icarus*, 376(1), 114840. Retrieved from  
 1096 <https://doi.org/10.1016/j.icarus.2021.114840>
- 1097 Styczinski, M. J., Vance, S. D., Niesyt, M., Lisitsyn, A., Daswani, M. M., Maru-  
 1098 siak, A. G., ... Bryant, A. S. (2022). *vancesteven/PlanetProfile: Fix man-*  
 1099 *tle compositions packaged in release* [Software]. Zenodo. Retrieved from  
 1100 <https://doi.org/10.5281/zenodo.7319838> doi: 10.5281/zenodo.7319838

- 1101 Tajeddine, R., Rambaux, N., Lainey, V., Charnoz, S., Richard, A., Rivoldini, A., &  
1102 Noyelles, B. (2014). Constraints on Mimas' interior from Cassini ISS libration  
1103 measurements. *Science*, *346*(6207), 322–324.
- 1104 Thomas, P., Tajeddine, R., Tiscareno, M., Burns, J., Joseph, J., Lored, T., ...  
1105 Porco, C. (2016). Enceladus's measured physical libration requires a global  
1106 subsurface ocean. *Icarus*, *264*, 37–47.
- 1107 Tobie, G., Mocquet, A., & Sotin, C. (2005). Tidal dissipation within large icy satel-  
1108 lites: Applications to Europa and Titan. *Icarus*, *177*(2), 534–549.
- 1109 Trumbo, S. K., Brown, M. E., & Hand, K. P. (2019). Sodium chloride on the surface  
1110 of Europa. *Science advances*, *5*(6), eaaw7123. doi: 10.1126/sciadv.aaw7123
- 1111 Turcotte, D. L., & Schubert, G. (2002). *Geodynamics*. Cambridge University Press.
- 1112 Tyler, G. L., Sweetnam, D. N., Anderson, J. D., Borutzki, S. E., Campbell, J. K.,  
1113 Eshleman, V. R., ... Wood, G. E. (1989). Voyager radio science observations  
1114 of Neptune and Triton. *Science*, *246*(4936), 1466–1473.
- 1115 Vance, S. D. (2017). *vancesteven/PlanetProfile: Release for use in reproducing re-*  
1116 *sults submitted to Journal of Geophysical Research - Planets* [Software]. Zen-  
1117 odo. Retrieved from <https://doi.org/10.5281/zenodo.844131> doi: 10  
1118 .5281/zenodo.844131
- 1119 Vance, S. D., Bouffard, M., Choukroun, M., & Sotin, C. (2014). Ganymede's in-  
1120 ternal structure including thermodynamics of magnesium sulfate oceans in  
1121 contact with ice. *Planetary and Space Science*, *96*, 62–70.
- 1122 Vance, S. D., & Brown, J. M. (2013). Thermodynamic properties of aqueous  $\text{MgSO}_4$   
1123 to 800 MPa at temperatures from  $-20$  to  $100^\circ\text{C}$  and concentrations to  $2.5 \text{ mol}$   
1124  $\text{kg}^{-1}$  from sound speeds, with applications to icy world oceans. *Geochimica et*  
1125 *Cosmochimica Acta*, *110*, 176–189.
- 1126 Vance, S. D., Hand, K. P., & Pappalardo, R. T. (2016). Geophysical controls of  
1127 chemical disequilibria in Europa. *Geophysical Research Letters*, *43*(10), 4871–  
1128 4879.
- 1129 Vance, S. D., Harnmeijer, J., Kimura, J., Hussmann, H., deMartin, B., & Brown,  
1130 J. M. (2007). Hydrothermal systems in small ocean planets. *Astrobiology*,  
1131 *7*(6), 987–1005.
- 1132 Vance, S. D., Panning, M. P., Stähler, S., Cammarano, F., Bills, B. G., Tobie, G., ...  
1133 Banerdt, B. (2018). Geophysical investigations of habitability in ice-covered



1134 ocean worlds. *Journal of Geophysical Research: Planets*, 123(1), 180–205. doi:  
 1135 10.1002/2017JE005341

1136 Vance, S. D., Styczinski, M. J., Bills, B. G., Cochrane, C. J., Soderlund, K. M.,  
 1137 Gómez-Pérez, N., & Paty, C. (2021). Magnetic induction responses of Jupiter’s  
 1138 ocean moons including effects from adiabatic convection. *Journal of Geophysi-  
 1139 cal Research: Planets*, 126(2), e2020JE006418. doi: 10.1029/2020JE006418

1140 Vitovtova, V. M., Shmonov, V. M., & Zharikov, A. V. (2014). The porosity trend  
 1141 and pore sizes of the rocks in the continental crust of the earth: Evidence  
 1142 from experimental data on permeability. *Izvestiya, Physics of the Solid Earth*,  
 1143 50(5), 593–602.

1144 Westall, F., & Brack, A. (2018). The importance of water for life. *Space Science Re-  
 1145 views*, 214(2), 1–23.

1146 Yu, C., Ji, S., & Li, Q. (2016). Effects of porosity on seismic velocities, elastic mod-  
 1147 uli and Poisson’s ratios of solid materials and rocks. *Journal of Rock Mechan-  
 1148 ics and Geotechnical Engineering*, 8(1), 35–49.

1149 Zannoni, M., Hemingway, D., Gomez Casajus, L., & Tortora, P. (2020). The gravity  
 1150 field and interior structure of Dione. *Icarus*, 345, 113713.

1151 Zimmer, C., Khurana, K. K., & Kivelson, M. G. (2000). Subsurface oceans on  
 1152 Europa and Callisto: Constraints from Galileo magnetometer observations.  
 1153 *Icarus*, 147(2), 329–347. doi: 10.1006/icar.2000.6456

1154 Zolotov, M. Y., & Kargel, J. S. (2009). On the chemical composition of Europa’s  
 1155 icy shell, ocean, and underlying rocks. In R. T. Pappalardo, W. B. McKinnon,  
 1156 & K. Khurana (Eds.), *Europa* (pp. 431–456). Tucson: University of Arizona  
 1157 Press.

# Supporting information for “*PlanetProfile*: Self-consistent interior structure modeling for terrestrial bodies in Python”

M. J. Styczinski<sup>1,2</sup>, S. D. Vance<sup>2</sup>, and M. Melwani Daswani<sup>2</sup>

<sup>1</sup>NASA Postdoctoral Program Fellow, Jet Propulsion Laboratory, California Institute of Technology, Pasadena, California, USA

<sup>2</sup>Jet Propulsion Laboratory, California Institute of Technology, Pasadena, California, USA

## Contents of this file

1. Text S1

2. Figures S1 to S5

3. Tables S1 to S5

## Introduction

This supplement contains comparisons between models of major moons generated with the latest version of *PlanetProfile* (v2.3.3, Styczinski et al., 2022) and analogous models from Vance et al. (2018), generated with the initial Matlab release of *PlanetProfile* (v1.0.0, Vance, 2017). The models we include here incorporate new features for improved self-consistency as described in the main text. An  $\text{H}_2\text{O}-\text{NH}_3$  EOS has not yet been implemented in the Python version of *PlanetProfile*, so those models are omitted from the comparison.

**Text S1.**

Figures S1–S5 compare several models of the moons Europa, Ganymede, Callisto, Enceladus, and Titan, as studied in Vance et al. (2018). Tables S1–S5 summarize the same models as those presented in the corresponding figures. Input Python files used to generate these figures and tables, output text files describing layer properties and model summaries, and comparison figure files are available as a Zenodo share at <https://doi.org/10.5281/zenodo.7318029>.

The models in this supplement have been adjusted from the default models described in the main text, with adjustments to the ocean melting temperature  $T_b$  such that the ice shell thickness  $z_b$  matches the models from Vance et al. (2018) as closely as possible. For some porous models, further adjustments were sometimes required in order to construct a valid model. In order to match the MoI for Titan and Callisto, we had to use extremely high rock porosities  $\phi_{\text{rock}}$  and pore closure pressures  $P_{c,\text{rock}}$ . This implies that the published MoI values for these bodies may be too high (due to a non-hydrostatic configuration) and a more realistic model for the required very-low-density rocky mantle will be important in future study. The configurations required to find MoI that lie within the uncertainty bounds as described in Section 1.1 imply that Titan and Callisto are not fully differentiated. A wider parameter space of models fits with the MoI for thinner ice shells, because the ocean density varies with the dissolved salt content, but the ice shell density does not. The low density of the ice shell drives down the MoI, adding tighter constraints on other parameters to match the high MoI for these bodies.

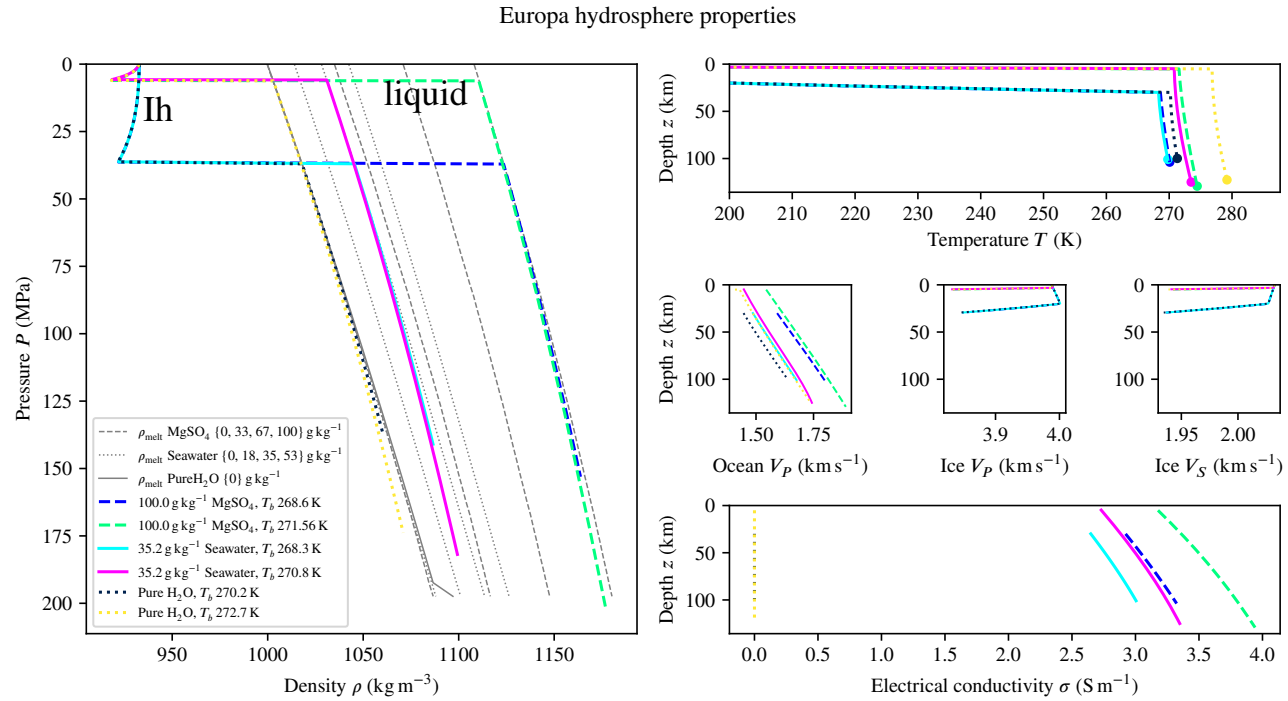


**Figure S1.** Updated *PlanetProfile* outputs for Europa, modeled after the conditions studied by Vance et al. (2018). Compare to Figure 7 from Vance et al. Refer to Table 5 (main text) for variable definitions.

	Europa	Europa	Europa	Europa	Europa	Europa
	100.0 g kg <sup>-1</sup> MgSO <sub>4</sub>	100.0 g kg <sup>-1</sup> MgSO <sub>4</sub>	35.2 g kg <sup>-1</sup> Seawater	35.2 g kg <sup>-1</sup> Seawater	Pure H <sub>2</sub> O	Pure H <sub>2</sub> O
Ocean comp.						
$M(\text{kg})$	$4.8000 \times 10^{22}$	$4.8000 \times 10^{22}$	$4.8000 \times 10^{22}$	$4.8000 \times 10^{22}$	$4.8000 \times 10^{22}$	$4.8000 \times 10^{22}$
$M_{\text{model}}(\text{kg})$	$4.7926 \times 10^{22}$	$4.7976 \times 10^{22}$	$4.7955 \times 10^{22}$	$4.7941 \times 10^{22}$	$4.7965 \times 10^{22}$	$4.7939 \times 10^{22}$
$C/MR^2$	$0.346 \pm 0.005$	$0.346 \pm 0.005$	$0.346 \pm 0.005$	$0.346 \pm 0.005$	$0.346 \pm 0.005$	$0.346 \pm 0.005$
$C_{\text{model}}/MR^2$	$0.34600^{+0.00042}_{-0.00042}$	$0.34606^{+0.00022}_{-0.00040}$	$0.34605^{+0.00047}_{-0.00047}$	$0.34618^{+0.00043}_{-0.00043}$	$0.34605^{+0.00026}_{-0.00048}$	$0.34601^{+0.00046}_{-0.00028}$
$\rho_{\text{rock,mean}}(\text{kg m}^{-3})$	3294	3436	3295	3443	3295	3438
$T_b(\text{K})$	268.6	271.56	268.3	270.8	270.2	272.7
$q_{\text{surf}}(\text{mW m}^{-2})$	16.1	98.2	16.1	103.2	16.2	99.5
$q_{\text{con}}(\text{mW m}^{-2})$	16.7	98.8	16.8	103.9	16.9	100.1
$\eta_{\text{con}}(\text{Pa s})$	$3.38 \times 10^{14}$	$2.82 \times 10^{14}$	$3.49 \times 10^{14}$	$3.05 \times 10^{14}$	$2.87 \times 10^{14}$	$2.51 \times 10^{14}$
$D_{\text{lh}}(\text{km})$	30.0	5.1	29.9	4.8	30.0	5.0
$D_{\text{ocean}}(\text{km})$	74.4	124.8	71.6	120.8	70.6	118.2
$\bar{\sigma}_{\text{ocean}}(\text{S m}^{-1})$	3.1	3.6	2.8	3.1	0.0	0.0
$R_{\text{surf}}(\text{km})$	1560.8	1560.8	1560.8	1560.8	1560.8	1560.8
$R_{\text{rock}}(\text{km})$	1456.4	1431.0	1459.3	1435.2	1460.2	1437.6
$R_{\text{core}}(\text{km})$	594.7	572.4	595.9	562.1	596.3	563.0

**Table S1.** Updated *PlanetProfile* outputs for Europa, modeled after the conditions studied

by Vance et al. (2018). Compare to Table 6 from Vance et al. Refer to Table 5 (main text) for variable definitions.

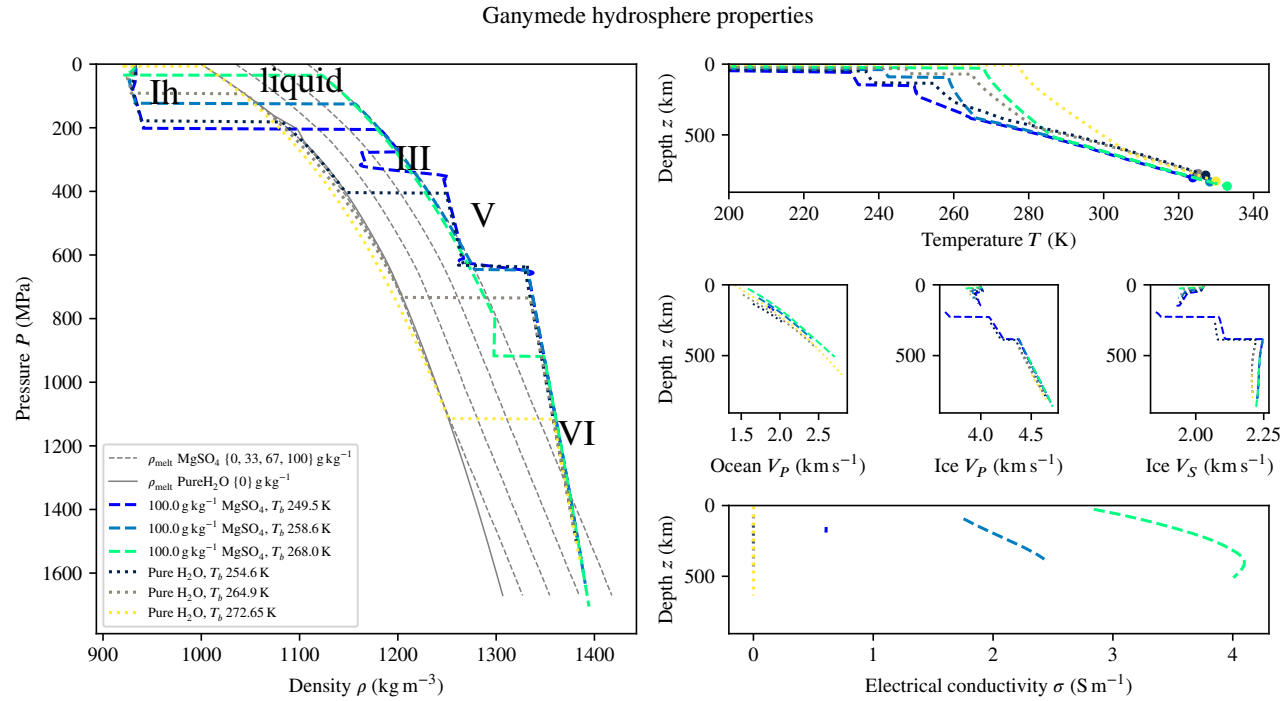


**Figure S2.** Updated *PlanetProfile* outputs for Ganymede, modeled after the conditions studied by Vance et al. (2018). Compare to Figure 5 from Vance et al. Refer to Table 5 (main text) for variable definitions.

	Ganymede	Ganymede	Ganymede	Ganymede	Ganymede	Ganymede
Ocean comp.	100.0 g kg <sup>-1</sup> MgSO <sub>4</sub>	100.0 g kg <sup>-1</sup> MgSO <sub>4</sub>	100.0 g kg <sup>-1</sup> MgSO <sub>4</sub>	Pure H <sub>2</sub> O	Pure H <sub>2</sub> O	Pure H <sub>2</sub> O
$M(\text{kg})$	$1.4819 \times 10^{23}$	$1.4819 \times 10^{23}$	$1.4819 \times 10^{23}$	$1.4819 \times 10^{23}$	$1.4819 \times 10^{23}$	$1.4819 \times 10^{23}$
$M_{\text{model}}(\text{kg})$	$1.4798 \times 10^{23}$	$1.4805 \times 10^{23}$	$1.4794 \times 10^{23}$	$1.4804 \times 10^{23}$	$1.4812 \times 10^{23}$	$1.4818 \times 10^{23}$
$C/MR^2$	$0.3115 \pm 0.0028$	$0.3115 \pm 0.0028$	$0.3115 \pm 0.0028$	$0.3115 \pm 0.0028$	$0.3115 \pm 0.0028$	$0.3115 \pm 0.0028$
$C_{\text{model}}/MR^2$	$0.31148^{+0.00014}_{-0.00006}$	$0.31155^{+0.00013}_{-0.00013}$	$0.31151^{+0.00012}_{-0.00009}$	$0.31156^{+0.00014}_{-0.00014}$	$0.31146^{+0.00014}_{-0.00014}$	$0.31152^{+0.00014}_{-0.00015}$
$\rho_{\text{rock,mean}}(\text{kg m}^{-3})$	3234	3220	3215	3226	3205	3551
$T_b(\text{K})$	249.5	258.6	268.0	254.6	264.9	272.65
$q_{\text{surf}}(\text{mW m}^{-2})$	10.4	16.5	18.4	13.2	22.4	97.7
$q_{\text{con}}(\text{mW m}^{-2})$	11.7	17.7	18.8	14.7	23.7	98.1
$\eta_{\text{con}}(\text{Pa s})$	$1.34 \times 10^{15}$	$6.82 \times 10^{14}$	$3.63 \times 10^{14}$	$8.10 \times 10^{14}$	$3.92 \times 10^{14}$	$2.52 \times 10^{14}$
$D_{\text{Ih}}(\text{km})$	151.4	93.4	26.4	134.3	69.8	5.1
$D_{\text{ocean}}(\text{km})$	40.7	287.0	483.6	134.4	375.7	630.9
$D_{\text{III}}(\text{km})$	34.4	-	-	-	-	-
$D_{\text{V}}(\text{km})$	157.6	-	-	119.7	-	-
$D_{\text{VI}}(\text{km})$	419.2	452.2	352.9	397.7	328.7	192.0
$\bar{\sigma}_{\text{ocean}}(\text{S m}^{-1})$	0.6	2.1	3.8	0.0	0.0	0.0
$R_{\text{surf}}(\text{km})$	2631.2	2631.2	2631.2	2631.2	2631.2	2631.2
$R_{\text{rock}}(\text{km})$	1828.0	1798.7	1768.3	1845.1	1857.0	1803.1
$R_{\text{core}}(\text{km})$	655.0	734.5	795.7	630.4	650.0	285.5

**Table S2.** Updated *PlanetProfile* outputs for Ganymede, modeled after the conditions studied

by Vance et al. (2018). Compare to Table 5 from Vance et al. Refer to Table 5 (main text) for variable definitions.

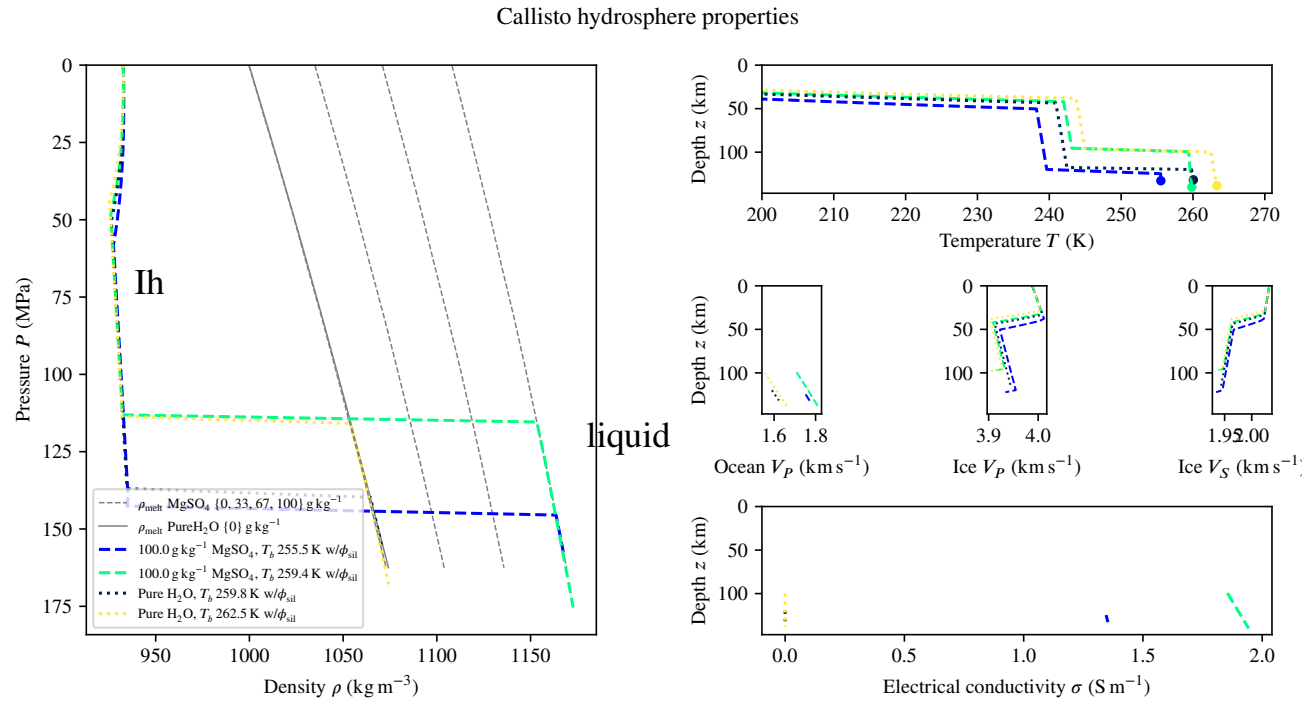


**Figure S3.** Updated *PlanetProfile* outputs for Callisto, modeled after the conditions studied by Vance et al. (2018). Compare to Figure 14 from Vance et al. Refer to Table 5 (main text) for variable definitions.



	Callisto	Callisto	Callisto	Callisto
Ocean comp.	100.0 g kg <sup>-1</sup> MgSO <sub>4</sub>	100.0 g kg <sup>-1</sup> MgSO <sub>4</sub>	Pure H <sub>2</sub> O	Pure H <sub>2</sub> O
$M(\text{kg})$	$1.0759 \times 10^{23}$	$1.0759 \times 10^{23}$	$1.0759 \times 10^{23}$	$1.0759 \times 10^{23}$
$M_{\text{model}}(\text{kg})$	$1.0756 \times 10^{23}$	$1.0759 \times 10^{23}$	$1.0757 \times 10^{23}$	$1.0756 \times 10^{23}$
$C/MR^2$	$0.3549^{+0.0042}_{-0.0148}$	$0.3549^{+0.0042}_{-0.0148}$	$0.3549^{+0.0060}_{-0.0166}$	$0.3549^{+0.0060}_{-0.0166}$
$C_{\text{model}}/MR^2$	$0.34147^{+0.00000}_{-0.00000}$	$0.34216^{+0.00000}_{-0.00202}$	$0.33842^{+0.00000}_{-0.00000}$	$0.33852^{+0.00000}_{-0.00000}$
$\rho_{\text{rock,mean}}(\text{kg m}^{-3})$	2000	2001	2000	2004
$T_b(\text{K})$	255.5	259.4	259.8	262.5
$q_{\text{surf}}(\text{mW m}^{-2})$	12.9	15.8	15.6	18.0
$q_{\text{con}}(\text{mW m}^{-2})$	14.3	17.2	17.3	19.6
$\eta_{\text{con}}(\text{Pa s})$	$8.90 \times 10^{14}$	$6.53 \times 10^{14}$	$5.50 \times 10^{14}$	$4.58 \times 10^{14}$
$D_{\text{lh}}(\text{km})$	124.7	99.4	119.9	99.8
$D_{\text{ocean}}(\text{km})$	9.5	42.1	13.3	40.1
$\bar{\sigma}_{\text{ocean}}(\text{S m}^{-1})$	1.3	1.9	0.0	0.0
$R_{\text{surf}}(\text{km})$	2410.3	2410.3	2410.3	2410.3
$R_{\text{rock}}(\text{km})$	2276.1	2268.8	2277.1	2270.4
$\phi_{\text{rock}}$	0.99	0.99	0.99	0.99

**Table S3.** Updated *PlanetProfile* outputs for Callisto, modeled after the conditions studied

by Vance et al. (2018). Compare to Table 10 from Vance et al. Refer to Table 5 (main text) for variable definitions.

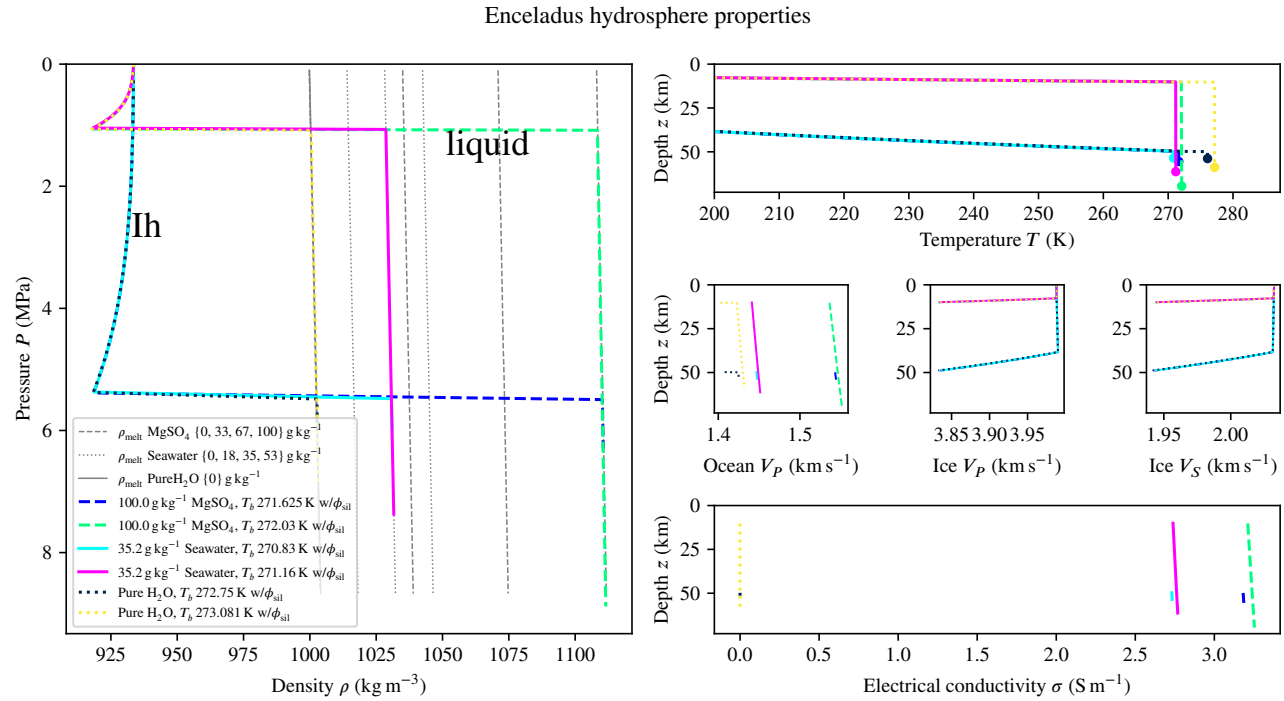


**Figure S4.** Updated *PlanetProfile* outputs for Enceladus, modeled after the conditions studied by Vance et al. (2018). Compare to Figure 10 from Vance et al. Refer to Table 5 (main text) for variable definitions.

	Enceladus	Enceladus	Enceladus	Enceladus	Enceladus	Enceladus
Ocean comp.	100.0 g kg <sup>-1</sup> MgSO <sub>4</sub>	100.0 g kg <sup>-1</sup> MgSO <sub>4</sub>	35.2 g kg <sup>-1</sup> Seawater	35.2 g kg <sup>-1</sup> Seawater	Pure H <sub>2</sub> O	Pure H <sub>2</sub> O
$M(\text{kg})$	$1.0802 \times 10^{20}$	$1.0802 \times 10^{20}$	$1.0802 \times 10^{20}$	$1.0802 \times 10^{20}$	$1.0802 \times 10^{20}$	$1.0802 \times 10^{20}$
$M_{\text{model}}(\text{kg})$	$1.0801 \times 10^{20}$	$1.0769 \times 10^{20}$	$1.0800 \times 10^{20}$	$1.0769 \times 10^{20}$	$1.0766 \times 10^{20}$	$1.0755 \times 10^{20}$
$C/MR^2$	$0.335 \pm 0.001$	$0.335 \pm 0.001$	$0.335 \pm 0.001$	$0.335 \pm 0.001$	$0.335 \pm 0.001$	$0.335 \pm 0.001$
$C_{\text{model}}/MR^2$	$0.33434^{+0.00136}_{-0.00006}$	$0.33459^{+0.00000}_{-0.00000}$	$0.33565^{+0.00000}_{-0.00154}$	$0.33445^{+0.00000}_{-0.00000}$	$0.33444^{+0.00000}_{-0.00007}$	$0.33409^{+0.00000}_{-0.00000}$
$\rho_{\text{rock,mean}}(\text{kg m}^{-3})$	2360	2485	2329	2399	2327	2371
$T_b(\text{K})$	271.625	272.03	270.83	271.16	272.75	273.081
$q_{\text{surf}}(\text{mW m}^{-2})$	9.3	47.4	9.3	47.9	9.4	47.4
$q_{\text{con}}(\text{mW m}^{-2})$	14.5	51.5	14.5	52.0	14.5	51.5
$\eta_{\text{con}}(\text{Pa s})$	$2.54 \times 10^{14}$	$2.48 \times 10^{14}$	$2.75 \times 10^{14}$	$2.71 \times 10^{14}$	$2.27 \times 10^{14}$	$2.24 \times 10^{14}$
$D_{\text{lh}}(\text{km})$	49.9	10.2	49.7	10.1	49.8	10.2
$D_{\text{ocean}}(\text{km})$	6.4	60.1	4.6	52.0	4.9	49.4
$\bar{\sigma}_{\text{ocean}}(\text{S m}^{-1})$	3.2	3.2	2.7	2.8	0.0	0.0
$R_{\text{surf}}(\text{km})$	252.1	252.1	252.1	252.1	252.1	252.1
$R_{\text{rock}}(\text{km})$	195.9	181.8	197.8	190.0	197.5	192.5
$\phi_{\text{rock}}$	0.27	0.27	0.27	0.32	0.32	0.32

**Table S4.** Updated *PlanetProfile* outputs for Enceladus, modeled after the conditions studied

by Vance et al. (2018). Compare to Table 7 from Vance et al. Refer to Table 5 (main text) for variable definitions.

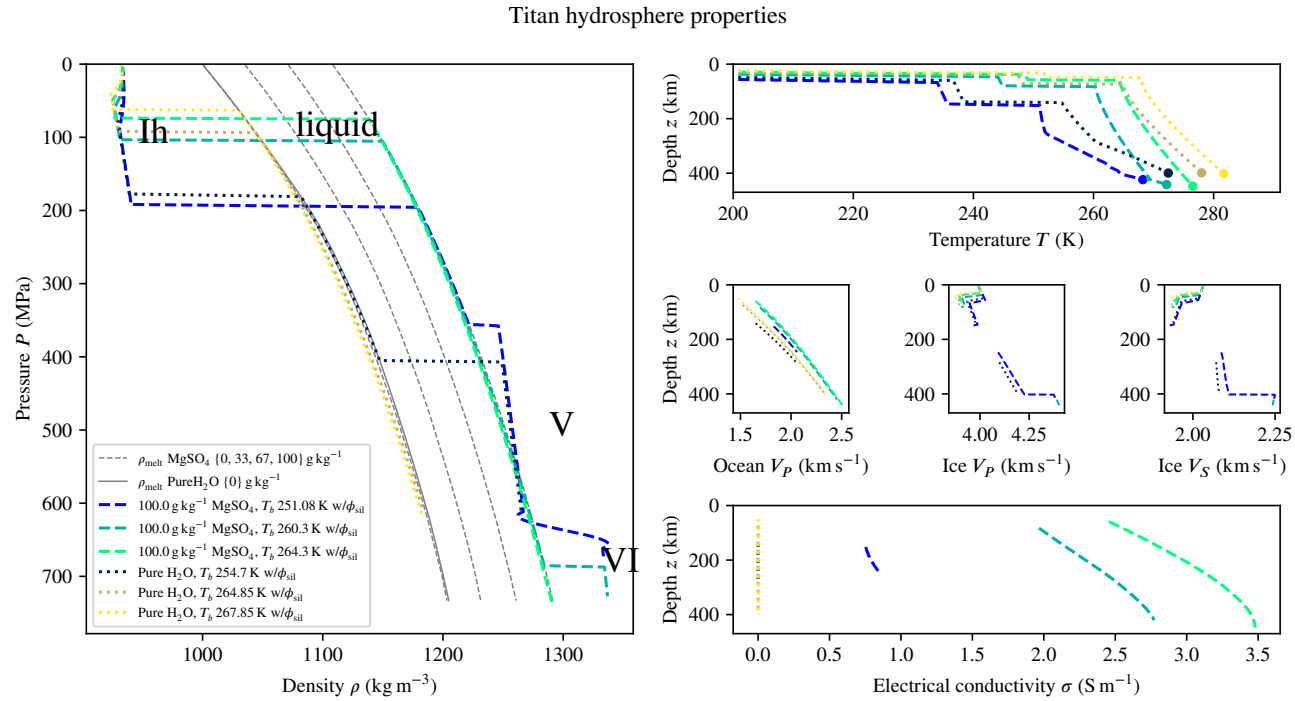


**Figure S5.** Updated *PlanetProfile* outputs for Titan, modeled after the conditions studied by Vance et al. (2018). Compare to Figure 12 from Vance et al. Refer to Table 5 (main text) for variable definitions.

	<b>Titan</b>	<b>Titan</b>	<b>Titan</b>	<b>Titan</b>	<b>Titan</b>	<b>Titan</b>
Ocean comp.	100.0 g kg <sup>-1</sup> MgSO <sub>4</sub>	100.0 g kg <sup>-1</sup> MgSO <sub>4</sub>	100.0 g kg <sup>-1</sup> MgSO <sub>4</sub>	Pure H <sub>2</sub> O	Pure H <sub>2</sub> O	Pure H <sub>2</sub> O
$M(\text{kg})$	$1.3452 \times 10^{23}$	$1.3452 \times 10^{23}$	$1.3452 \times 10^{23}$	$1.3452 \times 10^{23}$	$1.3452 \times 10^{23}$	$1.3452 \times 10^{23}$
$M_{\text{model}}(\text{kg})$	$1.3447 \times 10^{23}$	$1.3452 \times 10^{23}$	$1.3446 \times 10^{23}$	$1.3451 \times 10^{23}$	$1.3452 \times 10^{23}$	$1.3447 \times 10^{23}$
$C/MR^2$	$0.341^{+0.010}_{-0.020}$	$0.341^{+0.010}_{-0.020}$	$0.341^{+0.010}_{-0.020}$	$0.341^{+0.010}_{-0.020}$	$0.341^{+0.010}_{-0.020}$	$0.341^{+0.010}_{-0.020}$
$C_{\text{model}}/MR^2$	$0.32721^{+0.00000}_{-0.00053}$	$0.32960^{+0.00000}_{-0.00054}$	$0.33026^{+0.00000}_{-0.00037}$	$0.32567^{+0.00000}_{-0.00049}$	$0.32611^{+0.00000}_{-0.00055}$	$0.32638^{+0.00000}_{-0.00055}$
$\rho_{\text{rock,mean}}(\text{kg m}^{-3})$	2427	2429	2429	2410	2411	2410
$T_b(\text{K})$	251.08	260.3	264.3	254.7	264.85	267.85
$q_{\text{surf}}(\text{mW m}^{-2})$	10.1	16.5	20.8	12.0	20.4	24.8
$q_{\text{con}}(\text{mW m}^{-2})$	11.4	17.7	21.8	13.4	21.6	25.8
$\eta_{\text{con}}(\text{Pa s})$	$1.10 \times 10^{15}$	$5.88 \times 10^{14}$	$4.33 \times 10^{14}$	$7.62 \times 10^{14}$	$3.74 \times 10^{14}$	$3.12 \times 10^{14}$
$D_{\text{lh}}(\text{km})$	151.9	82.8	59.3	140.9	73.8	49.9
$D_{\text{ocean}}(\text{km})$	95.8	338.3	389.3	143.1	326.1	352.9
$D_{\text{V}}(\text{km})$	155.3	-	-	116.5	-	-
$D_{\text{VI}}(\text{km})$	21.7	21.8	-	-	-	-
$\bar{\sigma}_{\text{ocean}}(\text{S m}^{-1})$	0.8	2.4	3.1	0.0	0.0	0.0
$R_{\text{surf}}(\text{km})$	2574.7	2574.7	2574.7	2574.7	2574.7	2574.7
$R_{\text{rock}}(\text{km})$	2150.0	2131.9	2126.2	2174.2	2174.9	2172.0
$\phi_{\text{rock}}$	0.90	0.90	0.90	0.90	0.90	0.90

**Table S5.** Updated *PlanetProfile* outputs for Titan, modeled after the conditions studied

by Vance et al. (2018). Compare to Table 8 from Vance et al. Refer to Table 5 (main text) for

variable definitions.

## References

- 39 Styczinski, M. J., Vance, S. D., Niesyt, M., Lisitsyn, A., Daswani, M. M., Marusiak, A. G.,  
40 ... Bryant, A. S. (2022). *vancesteven/PlanetProfile: Fix mantle compositions packaged in*  
41 *release* [Software]. Zenodo. Retrieved from <https://doi.org/10.5281/zenodo.7319838>  
42 doi: 10.5281/zenodo.7319838
- 43 Vance, S. D. (2017). *vancesteven/PlanetProfile: Release for use in reproducing results submitted*  
44 *to Journal of Geophysical Research - Planets* [Software]. Zenodo. Retrieved from [https://](https://doi.org/10.5281/zenodo.844131)  
45 [doi.org/10.5281/zenodo.844131](https://doi.org/10.5281/zenodo.844131) doi: 10.5281/zenodo.844131
- 46 Vance, S. D., Panning, M. P., Stähler, S., Cammarano, F., Bills, B. G., Tobie, G., ... Banerdt,  
47 B. (2018). Geophysical investigations of habitability in ice-covered ocean worlds. *Journal*  
48 *of Geophysical Research: Planets*, 123(1), 180–205. doi: 10.1002/2017JE005341